

Offshore and Onshore Power curve characterization for ground-generation AWES

Markus Sommerfeld¹, Martin Dörenkämper², Jochem De Schutter³, and Curran Crawford¹

¹Institute for Integrated Energy Systems, University of Victoria, British Columbia, Canada

²Fraunhofer Institute for Wind Energy Systems, Oldenburg, Germany

³Systems Control and Optimization Laboratory IMTEK, Freiburg, Germany

Correspondence: Markus Sommerfeld (msommerf@uvic.ca)

Abstract.

Airborne wind energy systems (AWESs) are nominally envisaged to operate at altitudes above conventional wind turbines (WTs) and harvest energy from stronger winds aloft. This study investigates typical operating heights, power curves and annual energy production (AEP) of a ground-generation AWES with a wing area of $A_{wing} = 20\text{m}^2$. Various companies and researchers have proposed power curve characterizations for AWES, but no consensus for an industry-wide standard has been reached. A universal description of a ground-generation AWES power curve is difficult to define, because of complex tether and misalignment losses subject to alternating flight paths and wind conditions which lead to significant changes in the average cycle power. This study determines AWES power and AEP based on the `awebbox` optimal control model driven by representative onshore and offshore wind data. 10-minute mesoscale onshore and offshore wind conditions are analyzed with respect to atmospheric stability as well as annual and diurnal variation. To reduce the computational costs, these wind data are categorized using k-means clustering. The derived profiles cover a wide range of wind speeds and profile shapes which can not be replicated by standard logarithmic wind speed profiles. Wind data drives the optimization and result in distinct optimal AWES trajectories and power cycles.

Our data shows that optimal AWES operating heights are generally below 400 m and mostly around 200 m. We compare AWES power curve descriptions and estimate AEP based on wind speed probability distributions over various reference heights. These results are compared to quasi steady-state (QSS) AWES and WT reference models. The optimized power curves show a delay in rated wind speed which can be attributed to increased tether losses which are not captured by simplified model. Offshore AEP is generally higher than onshore, but lower wind shear weakens the argument for higher operating altitudes for AWES compared to conventional WT.

20 1 Introduction

Airborne wind energy systems (AWESs) aspire to harvest stronger and less turbulent winds at mid-altitude, here defined as heights above 100 m and below 1500 m, nominally beyond what is achievable with conventional wind turbines (WTs). The prospects of higher energy yield combined with reduced capital cost motivate the development of this novel class of renewable energy technology Lunney et al. (2017); Fagiano and Milanese (2012). Unlike conventional WTs, which have converged to

25 a single concept with three blades and a conical tower, several different AWES designs are under investigation by numerous
companies and research institutes Cherubini et al. (2015). These kite-inspired systems consist of three main components: a
flying wing or kite, a ground station and a tether to connect them. Various concepts compete for entry into the market. This
study focuses on the two-phase, ground-generation concept, also referred to as pumping-mode which is the main concept that
30 industry is investigating. During the reel-out phase the wing pulls a non-conductive tether from a drum on the ground which is
connected to a generator, thereby producing electricity. This is then followed by the reel-in phase during which the wing adjusts
its angle of attack to reduce aerodynamic forces and returns to its initial position. Other concepts such as fly-gen, aerostat or
rotary lift are not within the scope of this study Cherubini et al. (2015).

Since this technology is still at an early stage of development, validation and comparison of results is difficult. A standard-
ized power curve definition would enable comparison between different AWES concepts and to conventional wind turbines.
35 Together with the site-specific wind resource, power curves help wind park planners and AWES device manufacturers to es-
timate annual energy production (AEP) and determine financial viability Malz et al. (2020). As such this work supports the
development and implementation of this novel technology .

In contrast to a conventional WT, the power output of an AWES is highly dependent on the complete wind speed profile
(wind speed and direction variation with height) as system performance is governed by optimal operating trajectories over
40 the wind profile altitude range rather than primarily by a hub-height wind speed. Simple wind profile approximations using
logarithmic or exponential wind speed profiles, which are often erroneously applied beyond earths surface layer Optis et al.
(2016), might approximate long-term average conditions, but can not capture the broad variation of profile shapes that exist on
short timescales Emeis (2018).

They are therefore an inappropriate approximation to estimate instantaneous, diurnal and seasonal variation in electrical
45 power output. However, they are the standard in most AWES power estimation studies (e.g. Leuthold et al. (2018); Licitra et al.
(2019); De Schutter et al. (2018); Aull et al. (2020)). An alternative approach to estimating AWES energy production using the
ERA5 global reanalysis wind data set can be found in Schelbergen et al. (2020a).

AWES need to dynamically adapt their flight trajectory to changing winds in order to optimize power production. Wind ve-
locity profiles are governed by environmental, location-dependent conditions (e.g. surface roughness) and weather phenomena
50 on a multitude of temporal and spatial scales, subject to diurnal and seasonal patterns. The preferable means of determining
wind conditions are long-term, high resolution measurements, which at mid-altitudes can solely be achieved by long-range
LiDAR. Numerical mesoscale weather prediction models such as the weather research and forecasting model (WRF), which
is well known for conventional WT siting applications Salvação and Guedes Soares (2018); Dörenkämper et al. (2020), are
used to estimate wind conditions on time scales of a few minutes to years. These numerical simulations should be corrected for
55 systematic errors using measurements from light detection and ranging LiDAR during site assessment and deployment. Data in
this study are exclusively based on WRF mesoscale simulations, since measuring wind conditions at mid-altitudes is difficult
due to reduced data availability Sommerfeld et al. (2019a) and measurements are hard to find, typically being proprietary. We
compare conventional WT hub-height based power curves to optimal AWES performance for an onshore location in northern
Germany near the city of Pritzwalk Sommerfeld et al. (2019b) and an offshore location at the FINO3 research platform in the

60 North Sea. A key contribution of this paper is to account for the detailed variation in wind profiles and associated optimal flight trajectories in generating a power curve characteristic for AWES. To achieve this goal, we cluster the simulated wind velocity vectors using a k-means clustering algorithm. Through clustering, we avoid the excessive computational cost of computing optimal trajectories for each 10 min average profile, but maintaining a representative data set that encapsulates the important wind profile characteristics. The clustered profiles are also used to generate AEP estimates. Standard logarithmic wind profiles
65 are compared as reference calculations. Optimal AWES trajectories are generated using the `awebox` optimization framework, assuming simplified mass scaling.

In summary, this manuscript provides insight into typical onshore and offshore wind conditions up to 1000 m, their variation and the potential application of clustering to identify representative wind speed profiles and in turn yield more realistic power and energy estimation. Section 2 introduces the WRF model set-up and compares the onshore and offshore wind re-
70 source. Section 3 introduces the k-means clustering algorithm and summarizes results of clustered wind velocity profiles (both longitudinal and lateral wind components). These include cluster-averaged profiles and correlation with seasonal, diurnal and atmospheric stability. Section 4.3 introduces the `awebox` optimization framework. It summarizes aircraft, tether and ground station models as well as system constraints and initialization used to produce the results shown in section 5. These include flight paths and time series of various performance parameters, and a statistical analysis of tether length and operating altitude.
75 Furthermore, we compare power curve characterization, capacity factor and AEP estimates. Based on these results, an AWES power coefficient is defined to approximate AWES efficiency and power based on system size and wind speed. Finally, Section 6 concludes with an outlook and motivation for future work.

2 Wind data

This study compares the general AWES performance and power curves at a representative onshore and offshore location in
80 Europe (see fig 1). Wind conditions for the chosen years are assumed to be representative of that location. “Onshore” wind data at the Pritzwalk Sommersberg airport (lat: $53^{\circ}10'47.00''$ N, lon: $12^{\circ}11'20.98''$ E) in northern Germany and comprises 12 months of WRF simulation between September 2015 and September 2016. The area surrounding the airport mostly consists of flat agricultural land with the town of Pritzwalk to the south and is therefore a fitting location for wind energy generation (See Sommerfeld et al. (2019a) and Sommerfeld et al. (2019b) for details). The FINO3 research platform in the North Sea (lat:
85 $55^{\circ}11,7'$ N, lon: $7^{\circ}9,5'$ E) was chosen as a representative “offshore” location due to the proximity to several offshore wind farms and the amount of comprehensive reference measurements Peña et al. (2015). The offshore simulation covers the time frame between September 2013 and September 2014.

2.1 Mesoscale model

The mesoscale simulations in this study were carried out using the weather research and forecasting (WRF) model from
90 Skamarock et al. (2008). The onshore simulation was performed with version 3.6.1 before the 2018 release of WRF version

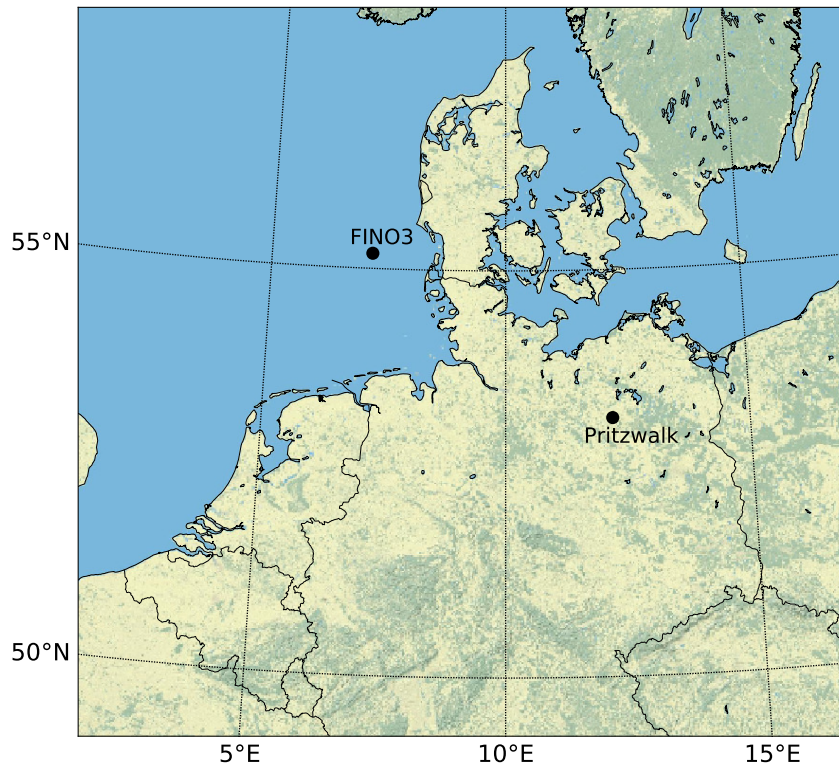


Figure 1. Map of northern Germany with the representative onshore (Pritzwalk) and offshore (FINO3) locations highlighted by black dots.

4.0.2¹ in which the offshore simulations were computed. The setup of the model has been adapted and constantly optimized for wind energy applications by the authors with the framework of various projects and applications in recent years Dörenkämper et al. (2015, 2017); Dörenkämper et al. (2020); Hahmann et al. (2020); Sommerfeld et al. (2019b).

The focus of this study is not on the detailed comparison between mesoscale models, but on AWES performance subject to representative onshore and offshore wind conditions determined based on clustered wind profiles (described in section 3). Both WRF models provide adequate wind data for for the assessment of AWES performance, even though the setup and time frame are different.

Both simulations consist of three nested domains centered around either the FINO3 met mast (see Figure 1) or the Pritzwalk Sommersberg airport. Atmospheric boundary conditions are defined by ERA-Interim Dee et al. (2011) for the onshore location and by ERA5 Hersbach and Dick (2016) reanalysis data for the offshore location, while sea surface parameters for the offshore

¹WRF model releases: <https://github.com/wrf-model/WRF/releases>

location are based on OSTIA Donlon et al. (2012). These data sets have proven to provide good results for wind energy relevant heights and sites Olauson (2018); Hahmann et al. (2020). Both simulations use the MYNN 2.5 level scheme for the planetary boundary layer (PBL) physics Nakanishi and Niino (2009). While the onshore simulation was performed in one 12 month simulations (01.09.2015 - 31.08.2016), the offshore simulation period consisted of 410 days (30.08.2013 - 14.10.2014) that were split into 41 simulations of 10 days each with an additional 24 hours of spin-up time per run. The data from the mesoscale models' sigma levels (terrain-following) were transformed to the geometric heights using the post-processing methodology described in Dörenkämper et al. (2020). Table 1 summarizes the key parameters of the model settings used in this study. All simulations were run on the *EDDY*² High-Performance Computing clusters at the University of Oldenburg.

Table 1. Key setup parameters of the onshore and offshore mesoscale model simulations

Model Parameter	Settings	
	Onshore	Offshore
WRF model version	3.5.1	4.0.2
time period	01.09.2015 - 31.08.2016	30.08.2013 - 14.10.2014
Reanalysis	ERA-Interim	ERA5 & OSTIA
Horizontal grid size (D01, D02, D03)	120x120, 121x121, 121x121	150x150, 151x151, 151x151
Resolution (D01, D02, D03)	27 km, 9 km, 3 km	18 km, 6 km, 2 km
Vertical levels	60 sigma levels (about 25 below 2 km)	60 sigma levels (about 25 below 2 km)
Nesting	1-way	1-way
Initialisation strategy	single run	240 h runs plus 24 h spinup time
Nudging	Analysis nudging (FDDA)	Analysis nudging (FDDA)
PBL scheme	MYNN level 2.5 scheme	MYNN level 2.5 scheme
Micro physics	Ferrier scheme	WRF Single-moment 5-class scheme
Long wave & shortwave radiation	RRTM & Dudhia	RRTMG scheme

2.2 Wind regime

Figure 2 depicts the wind roses of the annual wind conditions at 100 (top) and 500 m (bottom) height onshore (left) and offshore (right). The dominant wind direction at both locations is southwest, turning clockwise with increasing altitude.

Directional variability decreases and wind speed increases with height, following the expected trends in the northern hemisphere Arya and Holton (2001); Stull (1988). The average onshore wind direction turns about 14° between 100 and 500 m, whereas average offshore wind direction only veers approximately 5°. The offshore wind direction turns approximately 10° additional degrees above 500 m, resulting in roughly the same westerly wind direction at high altitudes at around 1000 m. Due

²EDDY: HPC cluster at the Carl von Ossietzky Universität Oldenburg, see: <https://www.uni-oldenburg.de/fk5/wr/hochleistungsrechnen/hpc-facilities/eddy/>

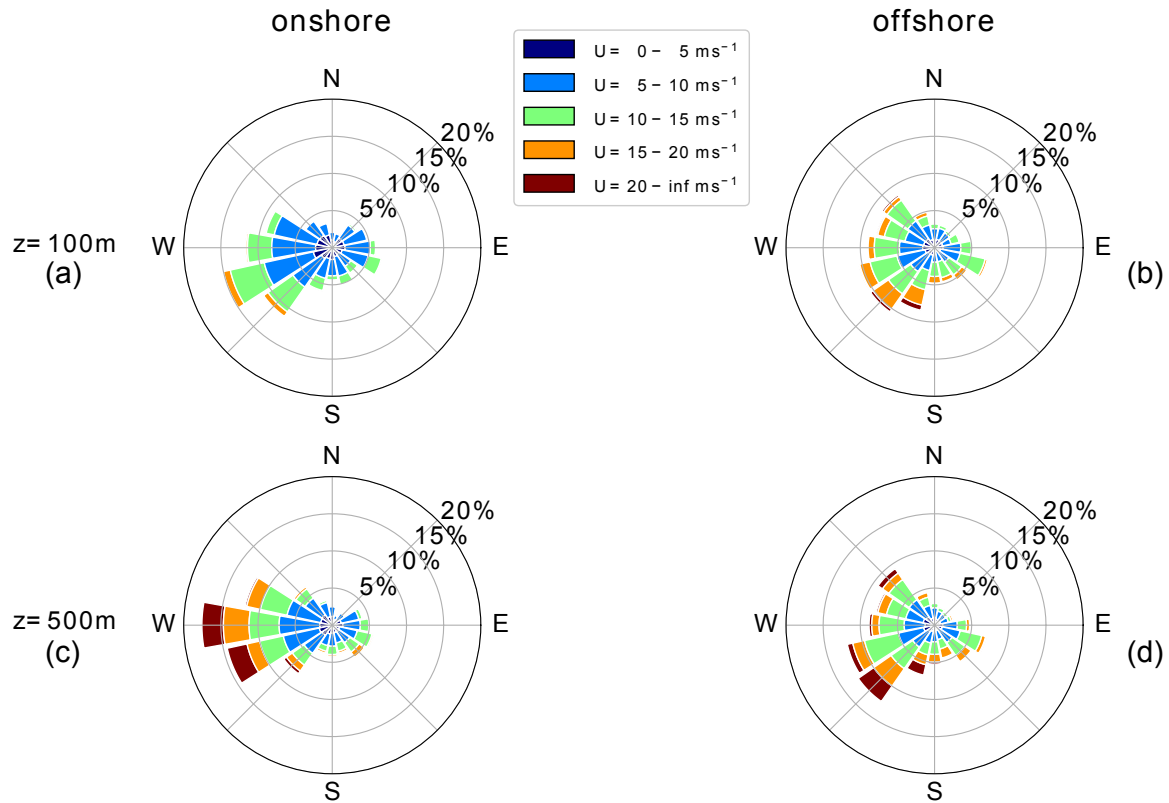


Figure 2. Annual wind direction and speed statistics at Pritzwalk (onshore) and FINO3 (offshore) presented as wind roses for 100 and 500 m.

to prevailing unstable conditions offshore, a strong mixing with height is found resulting in less veer across the heights investigated in this study. The wind shear at the offshore location is lower compared to the onshore location due to lower surface roughness.

Figure 3 shows the annual horizontal wind speed probability distributions at each individual height level for both locations. These distributions give an insight into the wind speed statistics at individual heights, but not into the statistics of the wind profile shapes, which are important for AWES power and trajectory optimization. The chosen nonlinear color range allows for the representation of the entire relative probability range. Onshore (left) wind speeds are relatively low and have a fairly narrow range below 300 m, due to dominant surface effects. Above this height the distribution broadens, but a high probability of low wind speeds remains for the full height range. The distributions show bi-modal characteristics caused by different atmospheric stratification. Low wind speeds are commonly associated with unstable and high wind speeds with neutral or stable atmospheric conditions (see sub-section 3.2).

Such multimodal distributions at higher altitudes are better described by the sum of two or more probability distributions, as standard Weibull or Rayleigh distributions can not capture this phenomenon Sommerfeld et al. (2019a). Offshore (right)

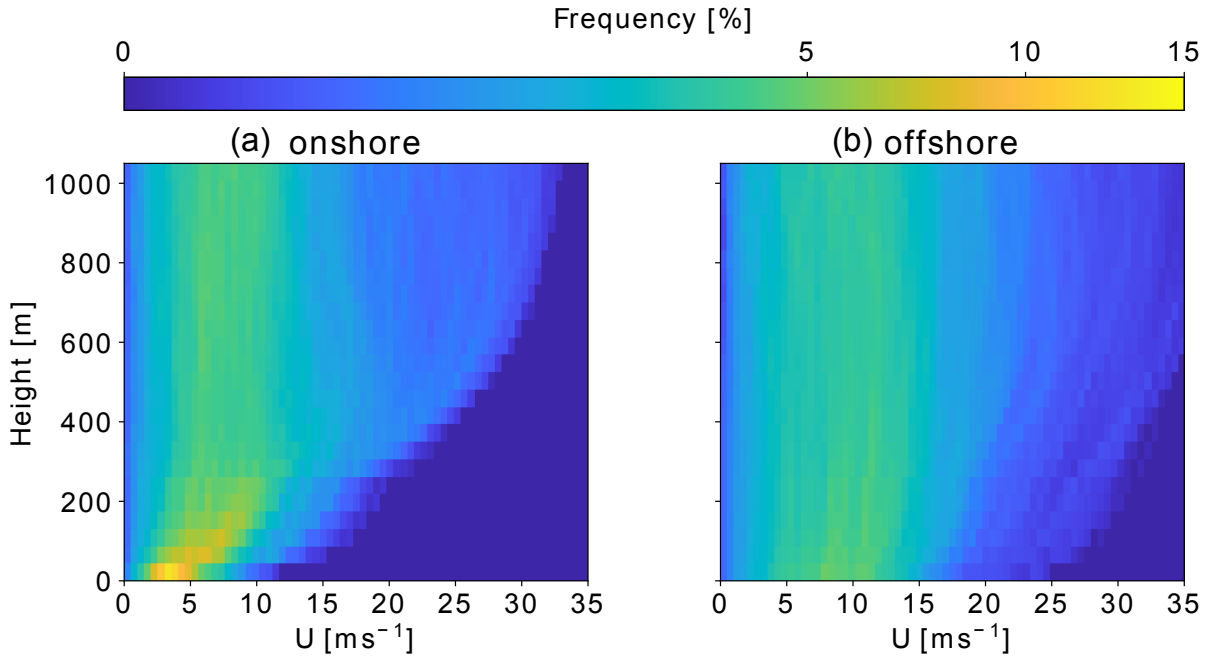


Figure 3. Comparison of WRF-simulated annual wind speed probability distribution at each height level between Pritzwalk (onshore left) and FINO3 (offshore right) up to 1000 m. A nonlinear color scheme was chosen to represent the high probability of low altitude onshore winds while still differentiating the lower, wide spread frequencies at higher altitudes.

wind speeds on the other hand have a wider distribution at all heights as they are less inhibited by surface effects. Similar to
 130 onshore, the offshore frequency distribution also shows a high probability of lower wind speeds (between 5-10 ms^{-1}) at all
 heights. Higher wind speeds at lower altitudes benefits conventional WT and weakens the argument for offshore AWES as one
 of their benefits would be to harness energy from the stronger winds at higher altitudes. Nevertheless, also AWES benefit from
 these higher wind speeds. Additional reasons for placing AWES offshore are safety and land use regulations and potential cost
 benefits of smaller support structure. If AWES can reliably operate autonomously they might still provide a cheaper source of
 135 electricity than conventional WT, due to their reduced material cost. Atmospheric stability of the boundary layer, which highly
 affects the wind speed profile shape, is commonly characterized using the Obukhov length \mathcal{L} Obukhov (1971); Sempreviva and
 Gryning (1996). Here the application is extended to mid-altitudes. \mathcal{L} is defined by the simulated friction velocity u_* , virtual
 potential temperature θ_v , potential temperature θ , kinematic virtual sensible surface heat flux Q_S , kinematic virtual latent heat
 flux Q_L , the von Kármán constant k and gravitational acceleration g :

$$140 \quad \mathcal{L} = \left(\frac{-u_*^3 \theta_v}{kg} \right) \left(\frac{1}{Q_S} + \frac{0.61}{Q_L \theta} \right). \quad (1)$$

Various stability classifications using Obukhov length are defined for different wind energy sites. Table 2 summarizes the Obukhov length bin widths Floors et al. (2011) and the frequency of occurrence of each stability class onshore and offshore, consistent with Sommerfeld et al. (2019b).

Neutral stratification occurs approximately 20% of the year at both locations. The lower heat capacity of the land surface leads to a faster heat transfer and a quicker surface cool-off which favors the development of stable stratification ($\approx 17\%$ onshore vs $\approx 6\%$ offshore). The offshore location has a higher probability of unstable conditions which is likely caused by a warmer ocean surface compared to the air above Archer et al. (2016).

Table 2. Stability classes based on Obukhov lengths Floors et al. (2011) and associated annual probability at Pritzwalk (onshore; 01.09.2015 - 31.08.2016) and FINO3 (offshore; 30.08.2013 - 14.10.2014), based on WRF results.

Stability class	\mathcal{L} [m]	onshore	offshore
Unstable (U)	$-200 \leq \mathcal{L} \leq -100$	7.27%	13.66%
Nearly unstable (NU)	$-500 \leq \mathcal{L} \leq -200$	7.09%	16.34%
Neutral (N)	$ \mathcal{L} \geq 500$	20.71%	22.82%
Nearly stable (NS)	$200 \leq \mathcal{L} \leq 500$	12.56%	5.15%
Stable (S)	$50 \leq \mathcal{L} \leq 200$	17.24%	6.20%
Very stable (VS)	$10 \leq \mathcal{L} \leq 50$	10.04%	2.96%
Other	$-100 \leq \mathcal{L} \leq 10$	25.09%	32.87%

Both unstable and stable conditions can lead to non-logarithmic and non-monotonic wind speed profiles. Unstable conditions are often accompanied by almost uniform wind speed profiles due to increased mixing, whereas low level jets (LLJs) can develop during the nocturnal stable onshore boundary layer Banta (2008). Both locations have a high chance of unassigned “other” conditions which are mostly associated with low wind speeds (see figure: 8).

3 Clustering of wind conditions

The power output of AWES highly depends on the wind velocity and its variation with height. Many temporal and spatial averages, correlations and approximations are used to describe the constantly varying wind conditions and their affect on wind energy converters. Instead of reverting to simple approximations such as the logarithmic wind speed profile, representative, WRF-simulated wind velocity profiles are chosen to compare AWES performance as realistically as possible.

Onshore (Pritzwalk) and offshore (FINO3) data are classified into groups to determine representative profiles. An accepted methodology to describe the near-surface atmosphere is atmospheric stability, commonly quantified by Obukhov length Obukhov (1971); Sempreviva and Gryning (1996) which exclusively uses surface data (see section 2.2 and equation 1). Previous studies Sommerfeld et al. (2019a, b) showed that Obukhov-length-classified wind speed profiles diverge with height, especially during neutral and stable conditions, which indicates vertically heterogeneous atmospheric stability and suggests that surface-based stability categorization is insufficient for higher altitudes. Clustering wind velocity profiles based on their

similarity was shown result in more cohesive profile groups Schelbergen et al. (2020b) (see figures A1 and A2). In contrast to classifying the wind regime by atmospheric stability, which requires temperature and heat flux data, clustering only uses wind data at multiple heights and groups profiles by similarity. Therefore, clustering can also be applied to wind-only measurements such as LiDAR.

The k-means clustering algorithm Pedregosa et al. (2011) used in this study was chosen for its ease of use and scalability, due to the high dimensionality of the data set. Many other algorithms produce similar results, but a comparison between clustering algorithms is beyond the scope of this research.

Before clustering, the two horizontal wind velocity components u and v , whose vertical variation define the wind velocity profile, are rotated such that the main wind component (average wind direction up to 500 m) u_{main} points in the positive x direction and the deviation $u_{\text{deviation}}$ is perpendicular to it, pointing in the positive y direction. This removes the directional dependency of the wind velocity profiles and results in more homogeneous clusters and simplifies the comparison of wind data and `awebox` results. It is analogous to assuming omnidirectional operation. The AWES still needs to adjust to changes in wind conditions with height.

The algorithm assigns each data point, in our case wind velocity profile up to 1000 m, which comprises approximately 30 heights and 2 directions, to one of k clusters represented by their respective cluster mean (also referred to as centroid). These centroids are arranged such that they minimize the sum of the Euclidean distances (also referred to as “inertia” or “within-cluster sum-of-squares”), i.e. the cost function of the algorithm, to every data point within each cluster. As such, the centroids are usually not actual data points, but rather the average of that cluster, and will at best coincide with a data point by chance. The cluster label number is random and does not have any mathematical meaning.

The variable k refers to the fixed, predefined number of clusters. The choice of k significantly affects the accuracy of the wind resource description, the resulting power and AEP predictions (see section 5.4) as well as the computational cost associated with clustering (pre-processing) and AWES trajectory optimization (processing). The elbow method and silhouette score indicate preferable choices of k . The elbow method (see fig: 4 - top left) compares the inertia trends as a function of k .

The parameter k is often chosen at a point where the inertia reduction becomes marginally small or decreases in a linear fashion with increasing number of clusters, often represented by a sharp bend or elbow in the inertia trend. A k of 20 seems to be a decent choice for the available data sets as inertia only decreases moderately for higher number of clusters which does not justify the additional computational cost. Absolute values of inertia are not a normalized metric and therefore scales with size of the considered data set. The silhouette coefficients on the other hand are normalized between -1 (worst) and 1 (best) and indicate the membership of a data point to its cluster in comparison to other clusters, i.e. proximity of each data point in one cluster to data points in neighboring clusters. A negative value suggests that a data point is assigned to the wrong cluster. The silhouette score (c figure 4) is the average of all silhouette coefficients for a fixed number of clusters k . Onshore (b) and offshore (d) silhouette coefficients for a representative k of 10. Each cluster is sorted by average wind speed up to 500 m and colored corresponding to the cluster centroids shown in figure 5. Silhouette coefficients (b,d) and the resulting silhouette score (c) indicate good cluster coherence at both locations. The impact of number of clusters on AEP is later discussed in sub-section 5.4.

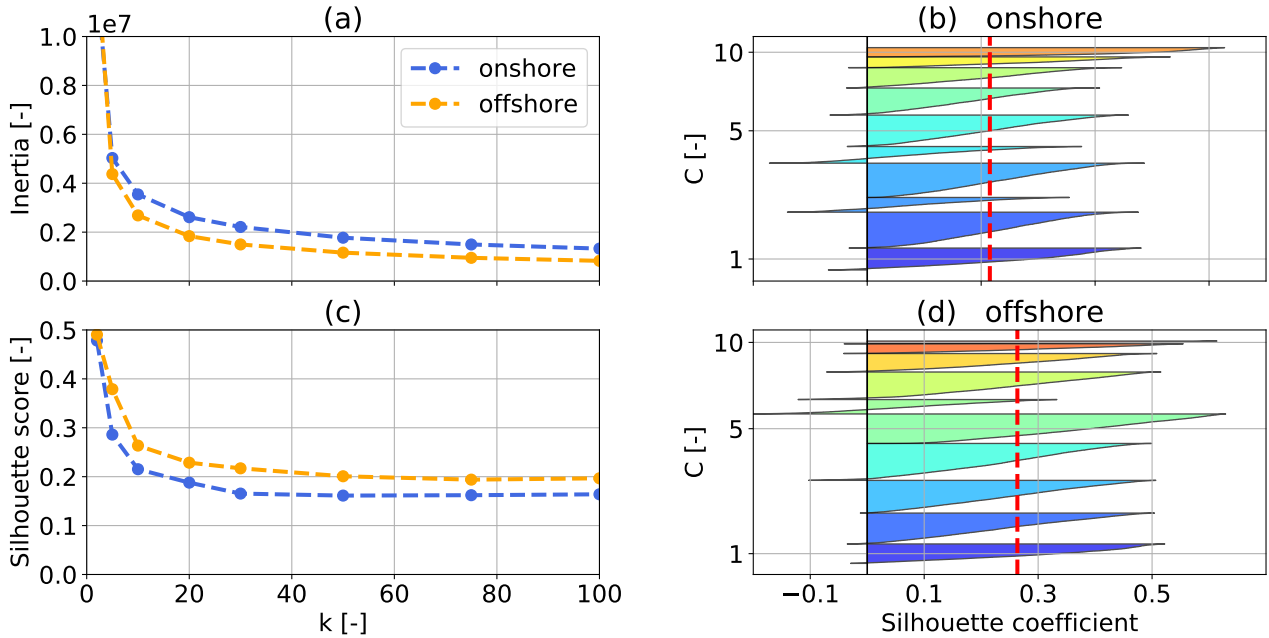


Figure 4. k-means clustering inertia over number of cluster k (a) for one year of onshore (blue) and offshore (orange) wind velocity profiles up to 1000 m. Silhouette score (c), average silhouette coefficients, over number number of cluster k for both locations. Onshore (b) and offshore (d) silhouette coefficients ($k=10$) express the distance to neighbouring clusters. The red dashed line represents the silhouette score.

3.1 Analysis of clustered profiles

For visualization purposes, the following sub-sections describe the wind conditions at both locations using only $k=10$ clusters, instead of the $k=20$ clusters chosen to analyze AWES performance in section 5. Figure 5 (top) shows the average wind speed profiles of the clustered wind velocity profiles, also referred to as centroids. The magnitude of the WRF-simulated wind velocity profiles that define their respective cluster are depicted in grey. Within a cluster, the wind speed profiles span a fairly narrow range of wind speeds except for a few outliers (see figure: A1, A1 in the appendix), indicating coherent clusters. Clusters are sorted by average centroid speed up to 500 m, represented by their colors and labels ($C = 1 - 10$).

As expected offshore (right) low altitude wind speeds are higher and wind shear is lower than onshore (left). Overall, offshore centroids are wider spread in comparison to the onshore profiles. The associated annual centroid frequency of occurrence for $k=10$ is shown below in figure 5. Wind speeds of the first and sixth offshore centroid decrease at higher altitude which could be caused by local or large-scale weather phenomenon. Both these clusters have a comparatively low probability. The first three onshore and offshore clusters exhibit very low wind shear with almost constant wind speed above 200 m. Onshore cluster 5, which seems to comprise of non-monotonic profiles as its centroid has a distinct LLJ nose at about 200 m, occurs about 5% of the time. Onshore centroids 7 and 8 also show a slight wind shear inversion at higher altitudes.

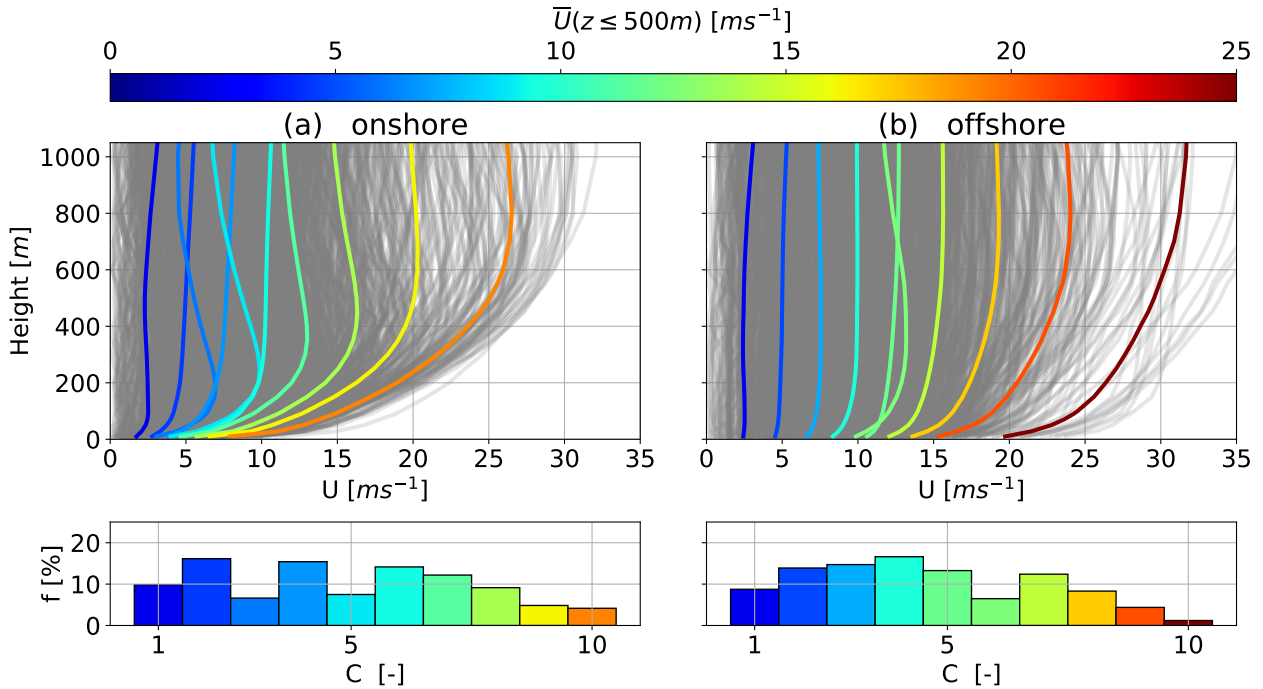


Figure 5. Onshore (left) and offshore (right) average annual wind speed profiles (or centroids) resulting from the k-means clustering process for $k = 10$ over height (top). Comprising WRF simulated wind velocity profiles depicted in grey. Centroids are sorted, labeled and colored in ascending order of average wind speed up to 500 m. The corresponding cluster frequency f for each cluster C is shown below.

Evidently, the wind speed magnitude plays a dominant role in clustering as the resulting centroids are nearly ordered in terms of speed, especially offshore. This can lead to profiles whose shape significantly differs from the one of the centroid to be assigned to a cluster due to similar average wind speed. A clearer wind profile shape distinction could have been achieved by
 215 normalizing the data before clustering it Molina-García et al. (2019); Schelbergen et al. (2020a). Normalization was deferred to simplify and clarify the clustering procedure as the focus of this manuscript is on the derivation and comparison of AWES
 power curves. With this application in mind, it is important to note that low speed profiles with an almost constant speed up to high altitudes add up to about 20-30 % of annual probability. This fact is often averaged out when only long term average wind
 speed profile shapes are considered and could lead to an overestimation of wind speeds at higher altitudes. AWES therefore
 220 need to be able to either operate under such low speed conditions or be able to safely land and take-off.

3.2 Analysis of clustered statistics

Figures 6 to 8 summarize the correlation between representative clusters ($k=10$) and monthly, diurnal and atmospheric stability for the onshore (top row) and offshore (bottom row) location. This reveals patterns within the data set and gives insight into

the wind prevailing regime. Clusters are sorted in ascending order of centroid average wind speed up to 500 m and colored accordingly. The corresponding centroids are shown in figure 5.

Both locations follow a distinct annual pattern (see figure 6) during which profiles associated with high wind speeds increase during the winter months and profiles with low wind speeds are predominantly found in summer. The two onshore and offshore clusters associated with the highest wind speed are almost exclusively present during November to February.

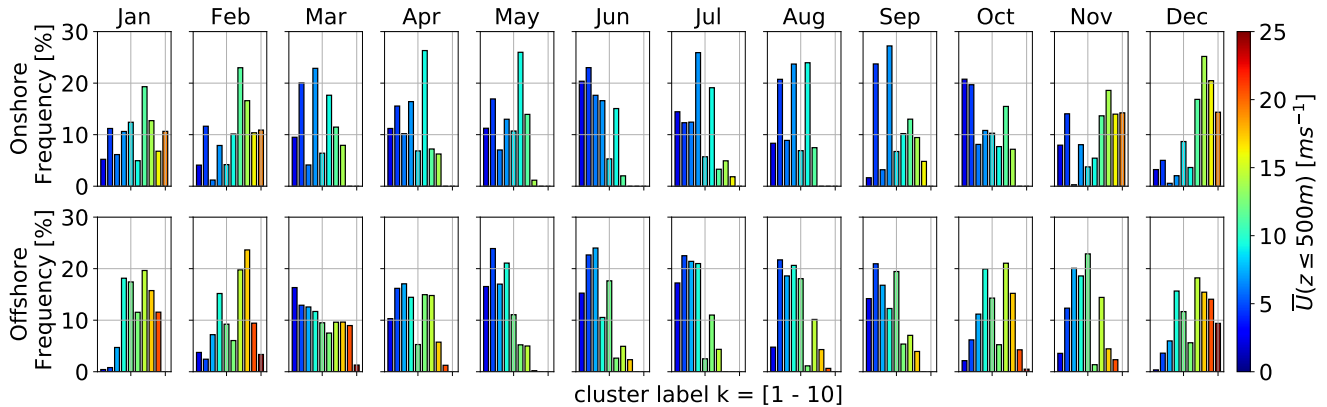


Figure 6. Monthly frequency of k-means clustered onshore (top) and (offshore) wind velocity profiles for a representative $k=10$. Clusters are sorted and colored by average wind speed up to 500 m. Centroids associated with each cluster can be found in figure 5.

Offshore data shows almost no diurnal variability (see figure 7) with only a slight increase of clusters associated with lower wind speeds during daytime. Onshore clusters on the other hand are more dependent on the diurnal cycle with a higher likelihood of low speed clusters after sunrise. The frequency of onshore cluster 5, which comprises a LLJ nose (see figure 5), drops to almost zero during daytime and increases during nighttime, substantiating the assumption that this cluster is associated with nocturnal LLJs.

The clustered wind velocity profiles and their associated speed and shape correlate with atmospheric stability as expected (see figure 8). Low wind speed clusters make up about 20% to 30% of the annual wind resource. These clusters exhibit Obukhov lengths close to zero (likely caused by very low friction velocity u_*) and are classified as “other” because they do not fall within one of the other atmospheric stability classes according to Floors et al. (2011) (see table 2). Unstable (U) and near unstable (NU) conditions are associated slightly higher wind speeds than “other” at both locations. The highest wind speeds develop during neutral (N) and near stable (NS) conditions. However, it should be acknowledged that strong winds driven by large pressure gradients tend to drive the stratification towards neutral. LLJ profiles associated with onshore cluster 5 are most likely to develop during stable (S) and very stable (VS) conditions.

In conclusion, k-means clustering is able to capture and reveal temporal variations in the wind regime as well as location specific wind profile shapes up to high altitudes. Wind speed magnitude seems to determine the resulting clusters more than profile shape. However, less common non-monotonic profiles with LLJs were identified. Normalizing the profiles before clustering

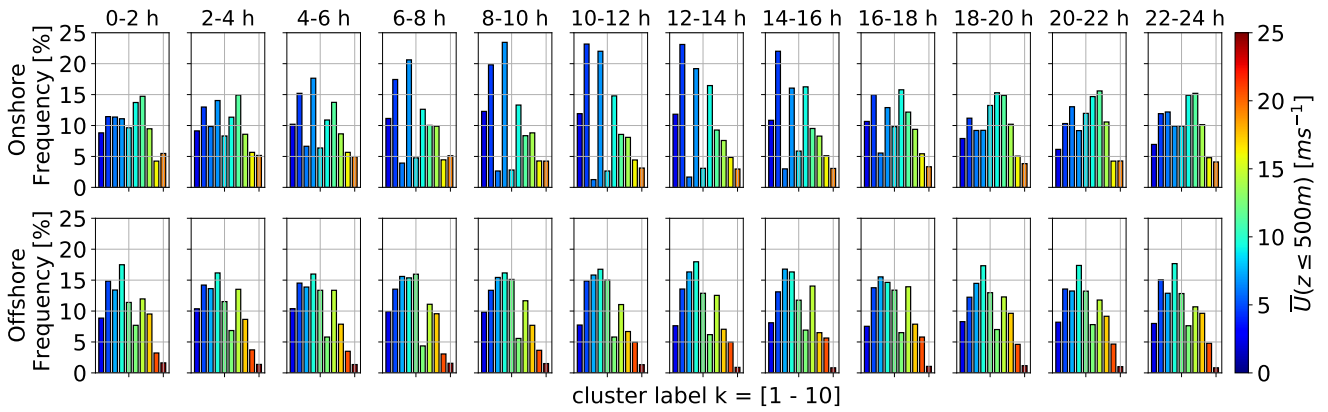


Figure 7. Diurnal frequency of k-means clustered onshore (top) and (offshore) wind velocity profiles for a representative $k=10$. Clusters are sorted and colored by average wind speed up to 500 m. Centroids associated with each cluster can be found in figure 5.

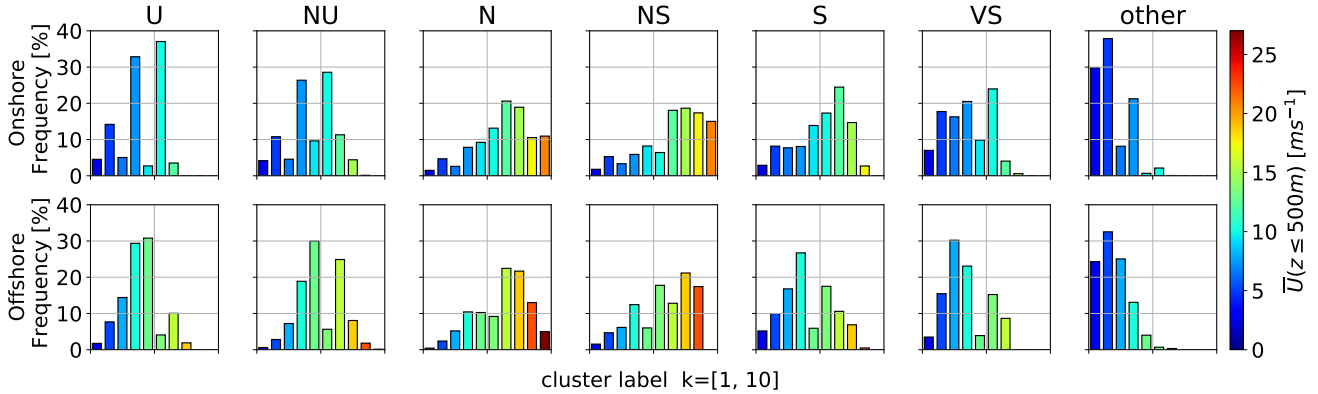


Figure 8. Atmospheric stability (U: unstable, NU: nearly unstable, N: neutral, NS: nearly stable, S: stable, VS: very stable) distribution of k-means clustered onshore (top) and (offshore) wind velocity profiles for a representative $k=10$. The associated stability classes are based on Obukhov length (see table 2). Clusters are sorted and colored by average wind speed up to 500 m. Centroids associated with each cluster can be found in figure 5.

245 should give more insight into the different vertical profile shapes. The corresponding cluster frequency follows the expected temporal trend and atmospheric stability association.

4 AWES model

This section introduces a quasi steady-state (QSS) reference ground-generation AWES model 4.1 and the dynamic trajectory optimization `awebox` model Leuthold et al. (2020) (sub-section 4.3, as well as a simple steady state WT model. These models

250 are later compared to `awebox` results in section 5. Both AWES models represent a scaled AP2 aircraft Malz et al. (2019); Ampyx (2020) connected to a ground station via a rigid tether. All models utilize the same simulated and clustered wind speed profiles described in section 3 as boundary conditions.

4.1 Engineering reference model

255 A QSS ground-generation AWES model (equation 2) Schmehl et al. (2013), adapted from Loyd's crosswind power approximation Loyd (1980), describes optimal power P_{opt} as a function of wind speed U , air density ρ_{air} and the resultant aerodynamic force coefficient c_{R} (equation 3). c_{R} is calculated from the aerodynamic lift c_{L} and total drag coefficient $c_{\text{D,total}}$, including wind and tether drag. The aerodynamic coefficients and derived variables such as glide-glide ratio and $c_{\text{R}}^3/c_{\text{D,total}}^2$ can be found in section 4.4 and figure 9.

$$P_{\text{opt}} = \frac{\rho_{\text{air}}(z)}{2} A_{\text{wing}} U(z)^3 c_{\text{R}} \left(\frac{c_{\text{R}}}{c_{\text{D,total}}} \right)^2 f_{\text{opt}} (\cos \theta \cos \phi - f_{\text{opt}})^2 \quad (2)$$

260
$$c_{\text{R}} = \sqrt{c_{\text{L}}^2 + c_{\text{D,total}}^2} \quad (3)$$

Aircraft and tether mass are neglected. Tether speed v_t is non-dimensionalized in the form of the reeling factor ($f = \frac{v_t}{U}$) with an optimal value of $f_{\text{opt}} = \frac{1}{3} \cos \theta \cos \phi$. The aircraft is assumed to move directly crosswind with a zero azimuth angle $\phi = 0$ relative to the wind direction. Elevation angle $\theta = \arcsin\left(\frac{z}{l_{\text{tether}}}\right)$ is derived from altitude z and tether length l_{tether} . The total drag coefficient $c_{\text{D,total}}$ determines the air resistance of the entire AWES in crosswind motion. It highly depends on the tether diameter d_{tether} and length l_{tether} , as well as the wing area A_{wing} and its aerodynamic drag coefficient $c_{\text{D,wing}}$ defined by the wing shape. Tether diameter $D_{\text{tether}} = 7.8\text{mm}$ is chosen such that rated wind speed is achieved at $v_{\text{rated}} = 10\text{ms}^{-1}$ (table 3). Figure 13 includes the QSS power curve which is defined by a combination of wind speed profile, tether length and operating height. We assume that the AWES flies at optimal power up to rated wind speed the maximum power. Beyond rated wind speed, power is capped at $P_{\text{rated}} = 260\text{kW}$ and tether length and operating height are adjusted to stay within this constraint. 270 Furthermore, figure 13 shows a simple WT model (equation 4) for reference.

$$P_{\text{WT}} = c_{\text{p}}^{\text{WT}} \frac{1}{2} \rho_{\text{air}} A_{\text{WT}} U^3 (z_{\text{WT}} = 100 \text{ m}) \quad (4)$$

Hub height z_{WT} is assumed to be 100 m for both onshore and offshore WT. Rotor diameter $D_{\text{WT}} \approx 35\text{m}$ and swept area of the turbine $A_{\text{WT}} \approx 1425\text{m}^2$ is chosen such that rated power, at a rated wind speed of $v_{\text{rated}} = 10\text{ms}^{-1}$, is equivalent to AWES rated power $P_{\text{rated}} = 260\text{kW}$, assuming a constant power coefficient of $c_{\text{p}}^{\text{WT}} = 0.45$.

This analysis utilizes the Ampyx AP2³ from Malz et al. (2019); Ampyx (2020). Aspect ratio is kept constant at $AR = 10$. The total drag coefficient $c_{D,\text{total}}$ highly depends on tether drag and therefore diameter d_{tether} and length l_{tether} , as well as the wing area A_{wing} and aerodynamic drag coefficient of the wing $c_{D,\text{wing}}$. We consider a straight, cylindrical tether with constant diameter and an aerodynamic tether drag coefficient $c_{D,\text{tether}}$ of 1.0, which could even be higher for braided tethers. Assuming
 280 a uniform wind, the line integral along the tether results in a total effective drag coefficient of:

$$c_{D,\text{total}} = c_{D,\text{wing}} + \frac{1}{4} \frac{d_{\text{tether}} l_{\text{tether}}}{A_{\text{wing}}} c_{D,\text{tether}} \quad (5)$$

See Houska and Diehl (2007); Argatov and Silvennoinen (2013); van der Vlugt et al. (2019) for details.

Figure 9 depicts the effect of tether drag on the $A_{\text{wing}} = 20\text{m}^2$ scaled AP2 aircraft for tether lengths up to $l_{\text{tether}} = 1000\text{m}$. Lift (a) and pitch moment (c) are assumed to behave linearly, while changes in the drag coefficient (b) are approximated
 285 quadratically. Tether drag is independent of aircraft angle of attack and therefore added to the zero-lift drag coefficient c_{D0} . Glide ratio $c_L/c_{D,\text{total}}$ (e) and Loyd power factor $c_R^3/c_{D,\text{total}}^2$ Loyd (1980) (f) not only decrease significantly with tether length, but optimal values move towards higher angle of attack. This effect will be less pronounced for larger wings due to beneficial scaling effects.

4.3 Dynamic optimization model

290 AWES need to dynamically adapt to changing wind conditions to optimize power generation. This can be formulated as a trajectory optimization problem which combines the interaction between tether, flying wing and ground station. For the purposes of this study, we analyze the mechanical power produced by a single tethered aircraft and assume a straight, rigid tether. Generating dynamically feasible and power-optimal AWES flight trajectories for given wind profiles is a nontrivial task given the nonlinear and unstable system dynamics and the presence of nonlinear flight envelope constraints. Optimal control
 295 methods are a natural candidate to tackle this problem, given their inherent ability to deal with nonlinear, constrained multiple-input-multiple-output systems. In periodic optimal control, an optimization problem is solved to compute periodic system state and control trajectories that optimize a system performance index (here average AWES power output \bar{P}) while satisfying the system dynamic equations. The initial and final state of the trajectory are freely chosen by the optimizer but must be equal to ensure periodic operation. We here apply this methodology to generate realistic single-wing, ground-generation AWES power
 300 curves and AEP estimation based on WRF-simulated wind velocity profiles using the `awebox`. Take-off and landing are not considered in this paper. Instead, only the production cycle, including reel-out as well as reel-in period, is optimized.

We consider a 6 degree of freedom (DOF) rigid-wing aircraft model which is connected to the ground via a rigid tether, thereby reducing the DOF to 5. It uses pre-computed quadratic approximations of the aerodynamic coefficients which are

³Aerodynamic coefficients can be found under: https://github.com/awebox/awebox/blob/develop/awebox/opts/kite_data/ampyx_data.py aircraft aerodynamic model

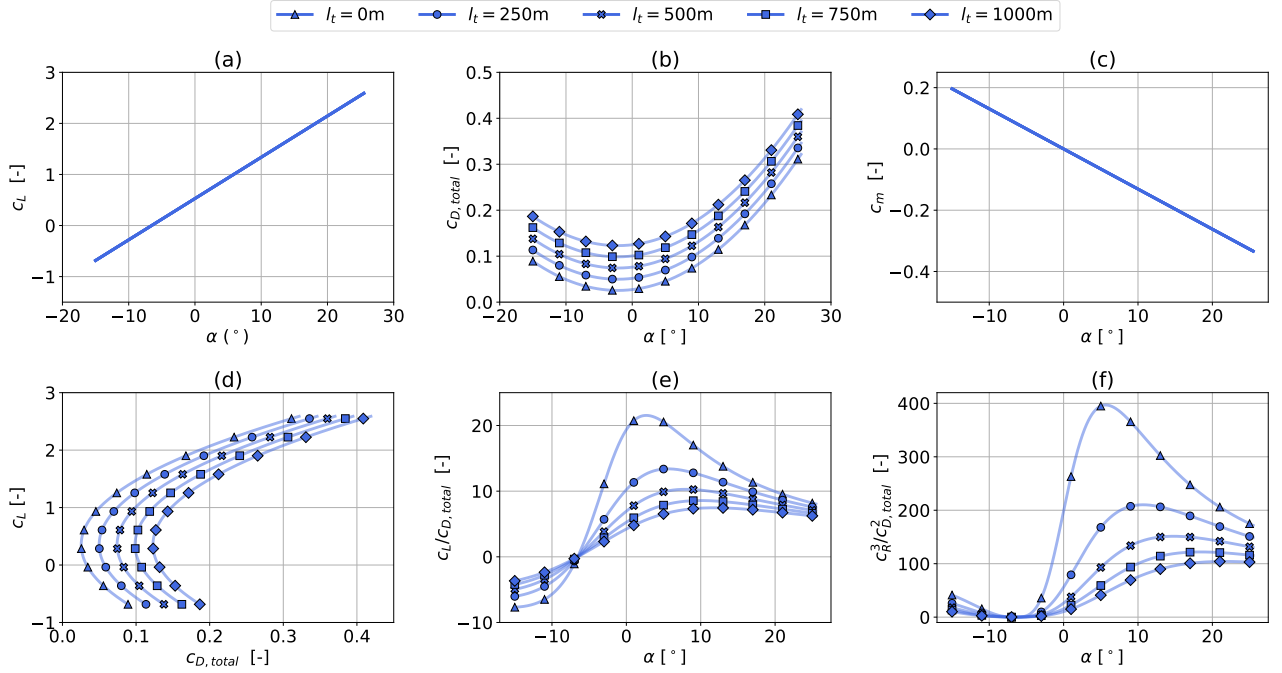


Figure 9. Ampyx AP2 reference wing aerodynamic lift c_L (a) and drag $c_{D,total}$ coefficients (b) Malz et al. (2019); Ampyx (2020), including tether drag according to equation 5, for a wing area A_{wing} of 20m^2 and tether diameter of $D_{tether} = 7.8\text{mm}$ (see table 3. Tether length varies between 250 m and 1000 m. (c) shows the pitch moment coefficient c_m as a function of angle of attack. The bottom figures display lift over drag (d), lift to drag ratio over angle of attack (e) and $c_L^3/c_{D,total}^2$ over angle of attack according to Loyd Loyd (1980).

controlled via aileron, elevator and rudder deflection rates Malz et al. (2019). The tether is controlled by the tether jerk $\ddot{\dot{l}}_{tether}$ from which tether acceleration \ddot{l}_{tether} , speed $\dot{l}_{tether} = v_{tether}$ and length (l_{tether}) are integrated. The tether is modeled as a single solid rod which can not be subjected to compressive forces De Schutter et al. (2019). The rod is divided into $n_{aero} = 10$ elements and tether drag is calculated individually for each element relative to apparent wind speed Bronnenmeyer (2018), with a tether drag coefficient of $c_D^{tether} = 1$. Wind profiles are implemented as 2D wind components rotated such that the main wind direction (u_{main} as defined by the average wind direction up to 500 m, compare section 3) is in positive x direction and the deviation from it in y direction. This is equivalent to assuming omnidirectional AWES operation with the wing still needing to adjust to changing wind conditions with height. Furthermore, we include a simplified atmospheric model based on international standard atmosphere to account for air density variation.

4.4 Aircraft model

Aircraft mass m and inertia J are scaled relative to wing span b with a mass scaling exponent κ (see equation 6), based on Galileo's square-cube law.

$$m_{\text{scaled}} = m_{\text{ref}} \left(\frac{b}{b_{\text{ref}}} \right)^\kappa; \quad J_{\text{scaled}} = J_{\text{ref}} \left(\frac{b}{b_{\text{ref}}} \right)^{\kappa+2} \quad (6)$$

Pure geometric scaling corresponds to $\kappa = 3$, but in reality, as has been seen for conventional WTs, design and material improvements occur with scaling over time. A review of the available literature containing system mass details was conducted to identify an appropriate mass scaling factor. The results are shown in Figure 10; actual and anticipated AWES scale bounded by $\kappa = 2.2 - 2.6$ (grey area). Based on a curve fit to the available published sizing study data, $\kappa = 2.4$ seems reasonable for future AWES development, but we leave a fulsome system AWES scaling study to future work. It can be assumed that lighter aircraft result in a lower cut-in wind speeds and higher power output.

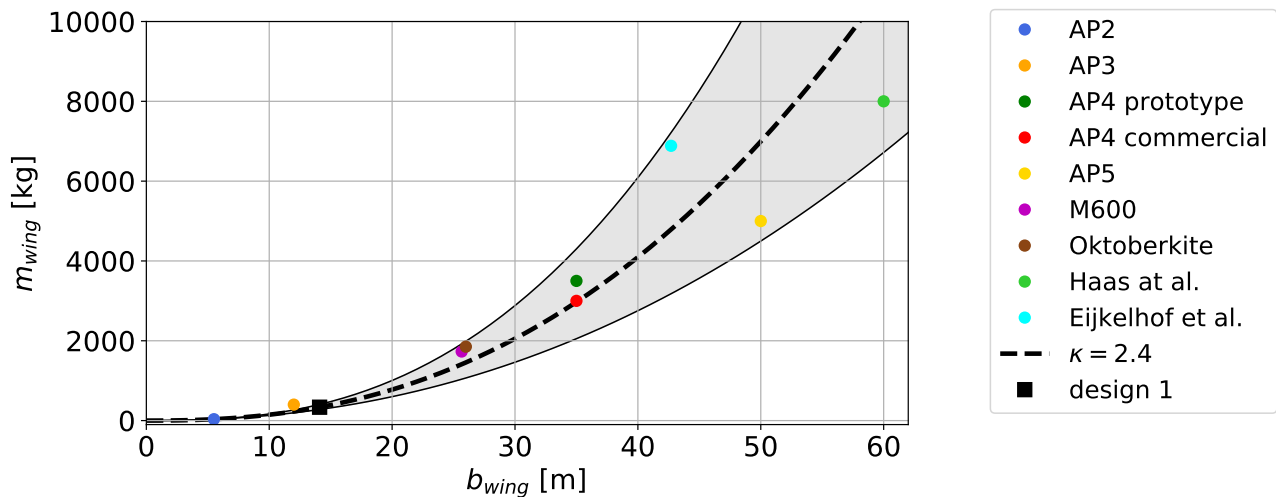


Figure 10. Curve fit of published sizing study AWES aircraft mass Haas et al. (2019); Kruijff and Ruitkamp (2018); Eijkelhof et al. (2020); Ampyx (2020); Echeverri et al. (2020). For these data mass scales within a scaling exponent range of $\kappa = 2.2 - 2.6$ (grey area). The chosen mass scaling exponent of $\kappa = 2.4$ is represented by a dashed line and the modeled design is highlighted by a black square.

4.5 Ground station model

The ground station is not explicitly modeled in our investigation, but implemented as a set of constraints which play a decisive role in the generated power of ground-generation AWES.

Table 3. Aircraft design parameters for AWES $A_{\text{wing}} = 20 \text{ m}^2$ analyzed in this study and for the original AP2 aircraft. Values in square brackets represent flight envelope bounds, which are implemented as inequality constraints of the optimization.

Parameter		AP2	design 1
Aircraft	wing area [m^2]	3	20
	wing chord [m]	0.55	1.42
	wing span [m]	5.5	14.1
	wing AR [-]	10	10
	kite mass [kg]	36.8	355
	β [$^\circ$]		[-15 : 15]
	max. air speed [ms^{-1}]		75
Tether	max. length [m]		2000
	speed [ms^{-1}]		[-15 : 10]
	max. acceleration [ms^{-2}]		[-10 : 10]
	diameter [mm]		7.8
	max. stress [Pa]		$3.6 \cdot 10^9$
	max. force [kN]		60
min operating altitude [m]			60

Using a simplified model, optimal reel-out speed can be estimated from elevation θ and azimuth angle ϕ : $v_{\text{out}} \approx \frac{1}{3} \cos \theta \cos \phi v_{\text{wind}}$ (section 4.1). Therefore, reel-out speed is expected to remain below 10 ms^{-1} as the wind speed hardly exceeds 20 ms^{-1} . A reel-out speed of $v_{\text{out}} = 15 \text{ ms}^{-1}$ and reel-in speed of $v_{\text{out}} = 10 \text{ ms}^{-1}$ were chosen, resulting in a reel-out to reel-in ratio of $\frac{2}{3}$ which is assumed to be within design limitations. A maximum tether acceleration of $\ddot{l} = 20 \text{ ms}^{-2}$ is imposed to comply with generator torque limits. The tether diameter is chosen such that rated power is achieved at $U_{\text{ref}} = 10 \text{ ms}^{-1}$. Constraints on the tether force enforce it to be positive whilst not exceeding the maximum tether stress, to which a safety factor of 3 is applied. This results in a tripling of the cross-sectional tether area. These ground station and tether constraints do not represent a fully optimized AWES, but rather a representative system.

4.6 Constraints

The tether constraints such as tether length, speed and force are summarized in table 3. Flight envelope constraints include limitation of aircraft acceleration, roll and pitch angle (to avoid collision with the tether) and angle of attack. The lift coefficient is assumed to be linear within this range. Furthermore, a minimal operating height of $z_{\text{min}} = 50 + \frac{A_{\text{wing}}}{2} \text{ m}$ is imposed for safety reasons.

4.7 Wind boundary condition

340 AWES trajectories depend on prevailing wind conditions as they greatly benefit from continuously adapting their operational altitude, tether speed and path to maximize power production and minimize losses. The above described AWESs were subjected to several different wind conditions to compare the impact on their trajectory, estimate the power curve and AEP. Logarithmic wind speed profiles (equation 7) with a roughness length of $z_0^{\text{onshore}} = 0.1$ and $z_0^{\text{offshore}} = 0.001$ are used as reference because they are the standard in the wind energy industry. A standard Rayleigh distribution (equation 8) with $U_{\text{onshore}}^{\text{ave}} = 10 \text{ ms}^{-1}$ and $U_{\text{offshore}}^{\text{ave}} = 12 \text{ ms}^{-1}$ is used to estimate AEP (sub-sections 5.3, 5.4) International Electrotechnical Commission (2010).

$$U_{\log} = U_{\text{ref}} \left(\frac{\log_{10}(z/z_0)}{\log_{10}(z_{\text{ref}}/z_0)} \right) \quad (7)$$

$$f_{\text{Rayleigh}} = \frac{2U}{U_{\text{avg}}} \exp - \left(\frac{U}{U_{\text{avg}}} \right)^2 \quad (8)$$

The reference wind speed U_{ref} at reference height $z_{\text{ref}} = 10 \text{ m}$ was varied from 3 to 19 ms^{-1} in steps of $\Delta U_{\text{ref}} = 2 \text{ ms}^{-1}$ to cover more than the common wind speed range. Results are compared to clustered, WRF simulated, onshore and offshore wind conditions in terms of power curve and AEP. We assume the same wind speed probability distribution for WRF wind profiles as well as the logarithmic reference wind speed profiles. Within each cluster, three WRF-calculated wind velocity profiles were chosen to assess the AWES power curve. Based on the average wind speed up to 500 m, which is used as a proxy for operating height ranges, the 5th, 50th and 95th percentile profile are chosen to represent the spectrum of wind conditions within each cluster. AWES performance analyses (section 5) and power curve estimation (section 5.3) are based on 3 wind profiles per k=5,10,20,50 clusters (section 3). The so derived power data points are interpolated over various reference wind speeds to derive AWES power curves. These interpolated power curves are then combined with probability distributions of these reference wind speeds to estimate AEP. Reference AEP is estimated from the annual summation of cluster-interpolated power. For this approach power is interpolated within each cluster linearly between p5,p50 and p95 and then summed up.

4.8 Problem formulation and solution

360 AWES trajectory optimization is a highly nonlinear and non-convex problem which likely has multiple local optima. Therefore, the particular results generated by a numerical optimization solver can only guaranty local optimality, and usually depend on the chosen initialization. This can result in unwanted or unrealistic AWES trajectories, which implies that the quality of all solutions needs to be evaluated a posteriori.

A periodic optimal control problem is formulated to maximize the average cycle power \bar{P} of a single AWES subject to equality (e.g. tether diameter) and inequality constraints described above De Schutter et al. (2019); Leuthold et al. (2018). The trajectory optimization problem is discretized into 100 intervals using direct collocation.

An initial guess is generated using a homotopy technique similar to Gros et al. (2013). A circular trajectory is estimated based on a fixed number of loops (here $n_{\text{loop}} = 5$) at a 15° elevation angle and the initial tether length. Initial aircraft speed

is based on the estimated duration of a single loop (here 10 sec). Previous analyses showed that the `awebbox`-estimated power output is insensitive to the number of loops and therefore flight time, at least for less than 10 loops. The homotopy technique initially fully relaxes the dynamic constraints using fictitious forces and moments to reduce model nonlinearity and coupling, improving the convergence of Newton-type optimization techniques. The constraints are then gradually re-introduced until the relaxed problem matches the original problem. The resulting nonlinear program (NLP) is formulated in the symbolic modeling framework CasADi for Python Andersson et al. (2019) and solved using the linear solver MA57 HSL (2020) in IPOPT Wächter and Biegler (2006).

5 Results

In this section we compare AWES trajectories and time series trends based on representative onshore (Pritzwalk) and offshore (FINO3) wind conditions. Building on that onshore and offshore operating height statistics and tether length trends are examined. AWES power curves are determined based on average cycle power and wind speeds at different reference heights. A quasi-steady reference AWES model (described in sub-section 4.1) as well as a WT model contextualize the results. Lastly, we compare performance in terms of annual energy production (AEP) for different number of clusters and reference heights.

5.1 Flight trajectory and time series results

This sub-section offers insight into typical optimized AWES flight trajectories. Figures 11 and A3 (appendix) compare the trajectories of representative onshore and offshore wind conditions between typical low and high wind speeds for an aircraft with a wing area of $A_{\text{wing}} = 20 \text{ m}^2$.

The top left sub-figure in figure 11 and A3 show the wind speed profiles U over altitude z with the operating height highlighted in color. The colored segments also depict the Lagrange polynomials that interpolate the WRF simulation data for optimization purposes. The bottom left figure shows a top view of the wind velocity profile (rotated horizontal u_{main} and $u_{\text{deviation}}$ wind component) in grey up to 1000 m displayed above as well as the part of the profiles corresponding to the height range swept by the aircraft in color. The two center plots show the optimized trajectory in side view (center top, x-z plane) and top view (center bottom, x-y plane).

When maximum tether force is reached the system starts to de-power while maintaining the same high tension (right, 1st from top in figures 11 and A3). Such trajectories often extend perpendicular to the main wind direction. This often results in odd or unexpected trajectories, even though these local minima are within the system constraints (roll rate etc.). De-powering by increasing the elevation angle is also possible and likely to happen, but harder to determine as it is not easily identifiable whether the elevation angle increased due to better wind conditions or to de-power the wing. Reducing the angle of attack (right, 3rd from top) while maintaining constant maximum tether force (right, 1st from top) can be observed in the highest onshore wind speed trajectory (green). During the production loops, the angle of attack constraint of the red and orange trajectories are active. The AWES angle of attack at the onshore location is generally higher than offshore (compare the third sub-figure on the right in figure 11 and A3). This can likely be attributed to the fact that onshore tether lengths are generally longer than offshore,

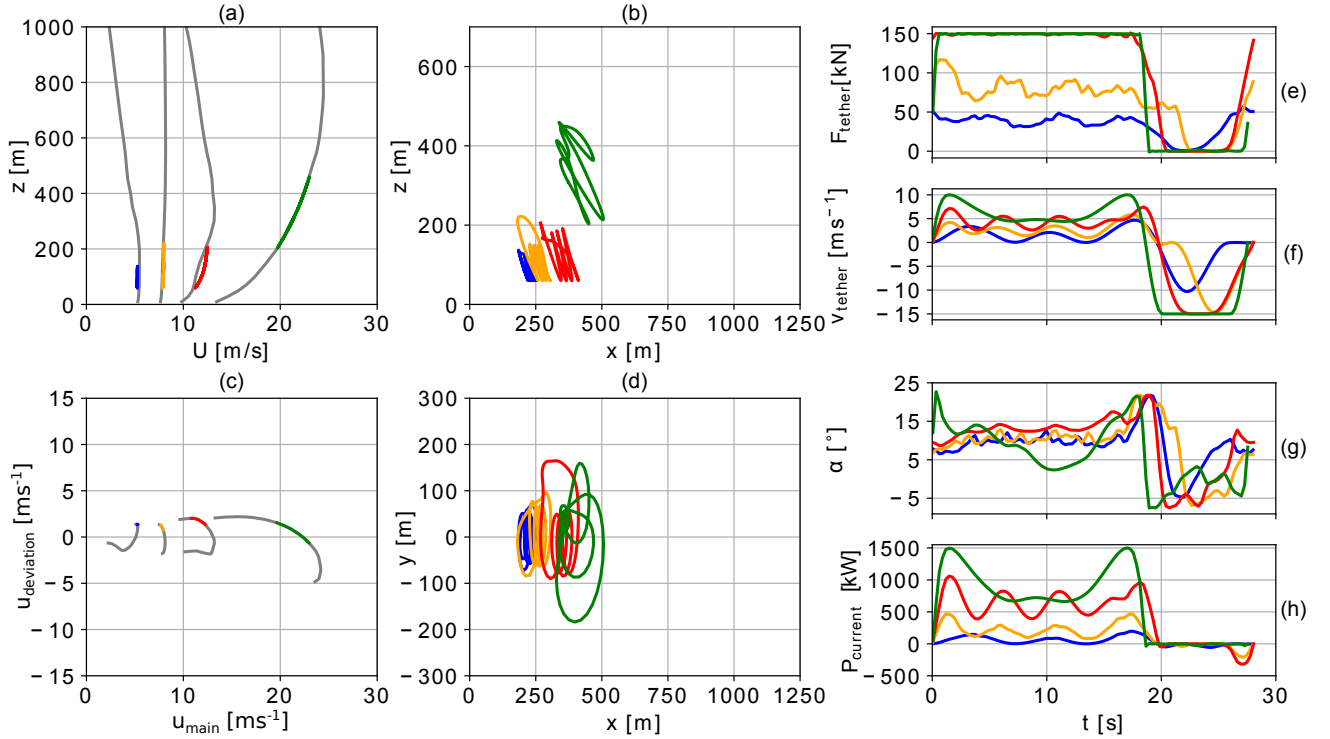


Figure 11. Representative wind speed profiles (left top), and hodograph (top view) of wind velocity up to 1000 m (left bottom). Wind profiles chosen to represent typical low (blue, orange), medium (red) and high wind speeds (green). Trajectories (center) in side and top view. Temporal variations of tether force F_{tether} (right 1st from top), tether speed v_{tether} (right 2nd from top), angle of attack α (right 3rd from top) and instantaneous power P_{current} (right, bottom) optimized based on clustered onshore wind speed profiles for a ground-generation AWES with a wing area of $A_{\text{wing}} = 20 \text{ m}^2$.

where beneficial wind conditions allow the AWES to operate at lower altitudes (see figure 12). As a result, the optimal c_L^3/c_D^2 shifts towards higher angle of attack.

The algorithm seems to always maximize tether force and vary tether speed (right 2nd from top) close to optimal reel-out speed ($v_{\text{out}} \approx \frac{1}{3} v_{\text{wind}}$ Loyd (1980)) to maximize average cycle power. At high wind speeds the trajectory starts to differ from
 405 its predefined shape with distinct loops and the system de-powers, which can be seen in the power development during the production phase (green). Trajectories for such high speed wind conditions without a tether force constraint, where the tether diameter is adjusted to the wind conditions, would be closer to the looping paths seen for lower wind speeds (blue, orange, red). The optimizer tries to keep the reel-in phase as short as possible, given tether speed and acceleration constraints. As a result, the reel-in tether speed reaches its limit for high wind speeds. The time history of instantaneous power P_{current} (right
 410 bottom) clearly distinguishes the production and consumption phase of pumping-mode (ground-generation) AWES. However, all optimized trajectories have a close to zero power usage during reel-in as they reduce the angle of attack to near zero lift

conditions. One commonality between all time series is that they almost all have the same flight time independent of location, wind speed or aircraft size. The flight time is almost solely determined by the initial number of loops, here five, used in the initialization procedure. Based on previous analyses, net mechanical AWES power output seems to be insensitive to the number of loops and flight time. The optimized trajectories result in almost zero tether force and therefore energy consumption during the reel-in phase. This might be different for real deployment, where a higher number of loops could be beneficial, because the reel-in time relative to reel-out time could be shorter.

5.2 Tether length, elevation angle and altitude

This sub-section compares tether lengths and operating altitudes for a wing size of $A_{\text{wing}} = 20 \text{ m}^2$. Data are based on the p5, p50, p95-th wind profiles of $k=20$ onshore (Pritzwalk) and offshore (FINO3) clusters (sub-section 4.7).

Figure 12 (a) illustrates the range of onshore (blue) and offshore (orange) AWES tether length l_{tether} of each wind velocity profile. The maximum is and minimum, highlighted by a square, are plotted over reference wind speed $U(z_{\text{ref}} = 100\text{--}300 \text{ m})$. Neither of the optimizations reaches the maximum tether length of $l_{\text{tether}}^{\text{max}} = 2000 \text{ m}$. Both locations show a trend towards longer tether lengths until rated wind speed. Beyond rated wind speed, tether lengths stay constant or even decrease as the system de-powers and tries to stay within constraints. The slightly lower tether length offshore is probably due to lower wind shear and more homogeneous wind regime (sub-section 2.2). The onshore data set displays multiple outliers, probably due to wind velocity profile variation, further supporting the need to dynamically adapt AWES operating conditions.

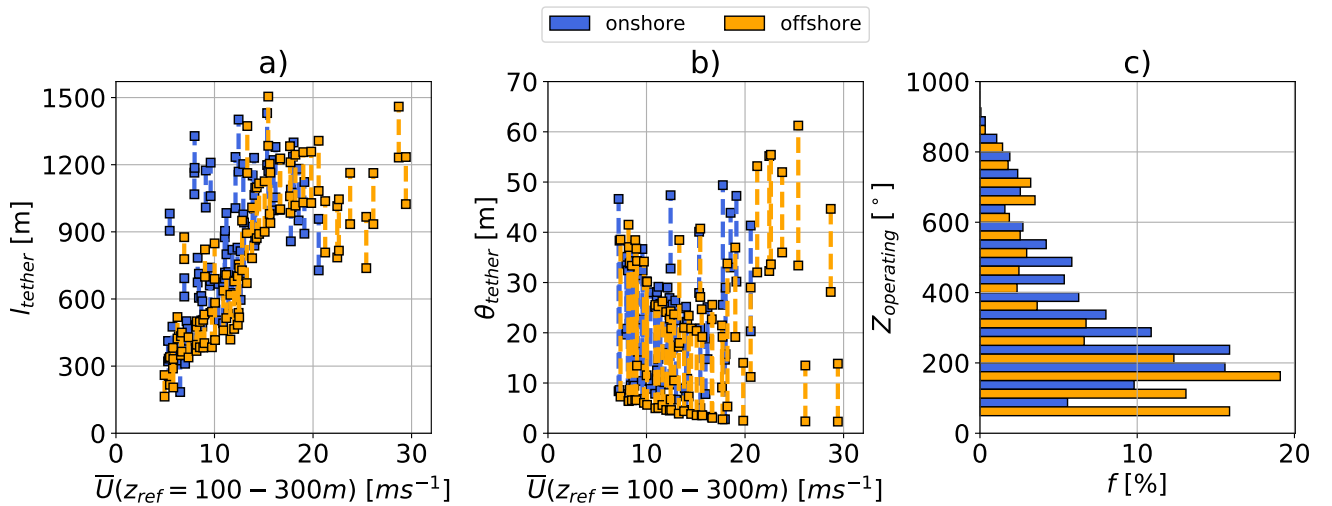


Figure 12. Tether length range (a) over reference wind speed $U(z_{\text{ref}} = 100 - 300 \text{ m})$ and frequency distribution of operating altitude (b) based on `awebox` trajectory optimization of $k=20$ onshore (blue) and offshore (orange) clusters.

Sub-figure (c) shows the elevation angle θ as a function of reference wind speed $U(z_{\text{ref}} = 100 - 300\text{m})$. As expected, the optimizer tries to keep elevation angle low to reduce misalignment losses. However, the increase in tether length with wind
 430 speed leads to an overall increase in operating heights. Both onshore and offshore follow a similar trend.

The right side of the figure 12 (c) shows the frequency distribution of operating altitude $z_{\text{operating}}$, calculated from the trajectory described in sub-section 5.1. Operating altitudes over the entire wind regime, both off- and onshore, are almost never higher than 500 m above ground, confirming findings in Sommerfeld et al. (2019a, b). Optimal operating heights at both locations is below 300 m for approximately 70% of the year. Larger or Multi-wing AWES could benefit from higher operating
 435 altitudes due to their higher lift to tether drag ratio and weight ratio, but more detailed analyses are required.

5.3 Power curve

Figure 13 (a, b) compares onshore (blue) and offshore (orange) optimized AWES power curves based on $k=20$ clustered (data points) and logarithmic wind speed profiles (dotted lines) to the AWES QSS model (solid line) as well as a simplified WT model (red line) described in sub-section 4.1. A cut-in wind speed of 5 m^{-1} is chosen as optimizations below this threshold
 440 did not converge. No cut-out wind speed was defined. Therefore, energy conversion is only limited by the wind resource. The presented AWES and WT reach rated power around $U_{\text{rated}} \approx 12\text{ms}^{-1}$. However, rated wind speed is visualized depending on reference height. Logarithmic wind speeds (equation 7) use roughness lengths of $z_0^{\text{onshore}} = 0.1$ and $z_0^{\text{offshore}} = 0.001$ (section 4.7). With average wind speed between 100 and 300 m as a reference wind speed (abscissa) the clustered power data form a relatively smooth power curve. This reference results in irregular WT and QSS power curve shapes. For the calculation of
 445 WT wind speed and energy distribution a reference height of 100m is used. The clustered power curve fit aligns well with optimization results for logarithmic wind speed profiles at this reference height.

Sub figures c and d show the AWES harvesting factor ζ from Diehl (2013) which expresses the estimated AWES power P relative to the total wind power through an area the same size as the wing P_{area} . A reference wind speed averaged over operational height $U_{\text{ref}}(z = 100 - 300)\text{m}$ is used to estimate ζ . At low wind speeds the optimization model finds higher power
 450 output than the QSS model. This is likely caused by the choice of reference wind speed which leads to a shift in these data points towards lower wind speeds.

$$\zeta = \frac{P}{P_{\text{area}}} = \frac{P}{\frac{1}{2}\rho_{\text{air}}A_{\text{wing}}U(z)^3} \leq \frac{4}{27}c_{\text{R}} \left(\frac{c_{\text{R}}}{c_{\text{D}}} \right)^2 \quad (9)$$

Sub-figures e and f show the wind speed probability distribution for the chosen average reference wind speeds between 100 and 300 m (bars), at 100 m WT hub-height (red line) and the standard Rayleigh distribution (dotted lines) with $U_{\text{onshore}}^{\text{ave}} =$
 455 10 ms^{-1} and $U_{\text{offshore}}^{\text{ave}} = 12\text{ ms}^{-1}$ (equation 8) International Electrotechnical Commission (2010). As expected, higher operating altitudes reach higher wind speeds. However, low wind speeds of less than 5 ms^{-1} still occur almost at the same frequency as at lower altitude, both onshore and offshore.

These distributions, together with the power curves, are used to generate the annual energy distribution in sub-figures g and h. In comparison to conventional WT, the AWES energy distribution is shifted towards higher wind speeds. For AWES to

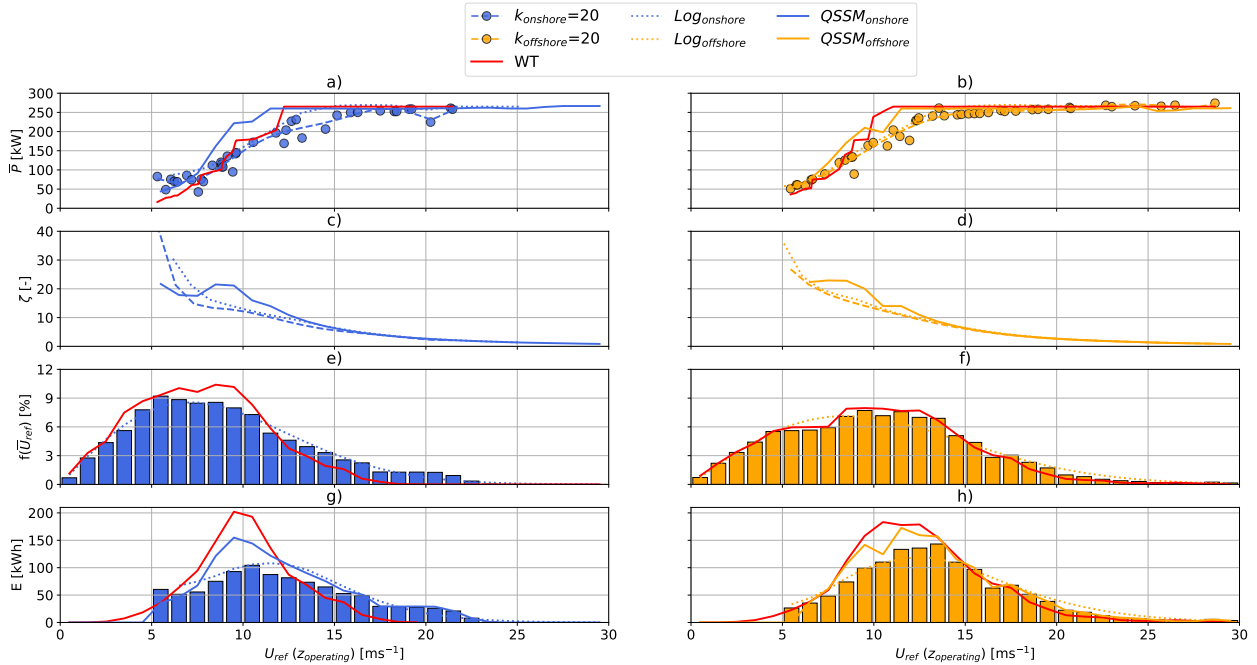


Figure 13. Onshore (blue) and offshore (orange) AWES power curves (a,b) over average wind speed between $z = 100 - 300$ m based on 3 wind profiles for each of the $k=20$ clusters. Simplified WT model (red lines), QSS AWES model (solid lines) and AWES subject to logarithmic wind boundary conditions (dotted lines) with rated wind speed of $v_{rated} = 10 \text{ m s}^{-1}$ and the same rated power for reference. Harvesting factor ζ (equation 9 shown in c, d). Annual energy distribution (e,f) based on power curves and WRF-simulated annual wind speed probability distributions (c,d) and standard Rayleigh distributions. International Electrotechnical Commission (2010).

460 convert power during these conditions, the flight path needs to be adjusted to de-power so that the AWES stays within material strength limitations.

In contrast to conventional WT with their fixed hub-height, AWES adapt their operating heights dynamically, which makes the choice of reference wind speed non-trivial. Due to many conceptually different AWES designs and the novelty of the technology, no generally accepted AWES power curve definition exists. Similarly, no standard wind resource model such as the Rayleigh or Weibull distribution for conventional wind has been defined. Figure 14 investigates the impact of different reference heights on AWES power curve representations (a,b)

465 These power curves are derived from curve fits of 3 wind velocity profiles within each of the $k=20$ onshore (blue) and offshore (orange) clusters. Together with differing wind speed probability distributions (c,d) this leads to varying annual energy distribution (e,f) and therefore AEP (sub-section 5.4). The area underneath the distribution accumulates to the annual energy production (AEP) further analyzed in sub-section 5.4. WT data with a reference wind speed at $z = 100\text{m}$ (black dashed lines) and QSS data with an average reference wind speed between $100 \leq z \leq 300\text{m}$ (solid lines) are included for comparison.

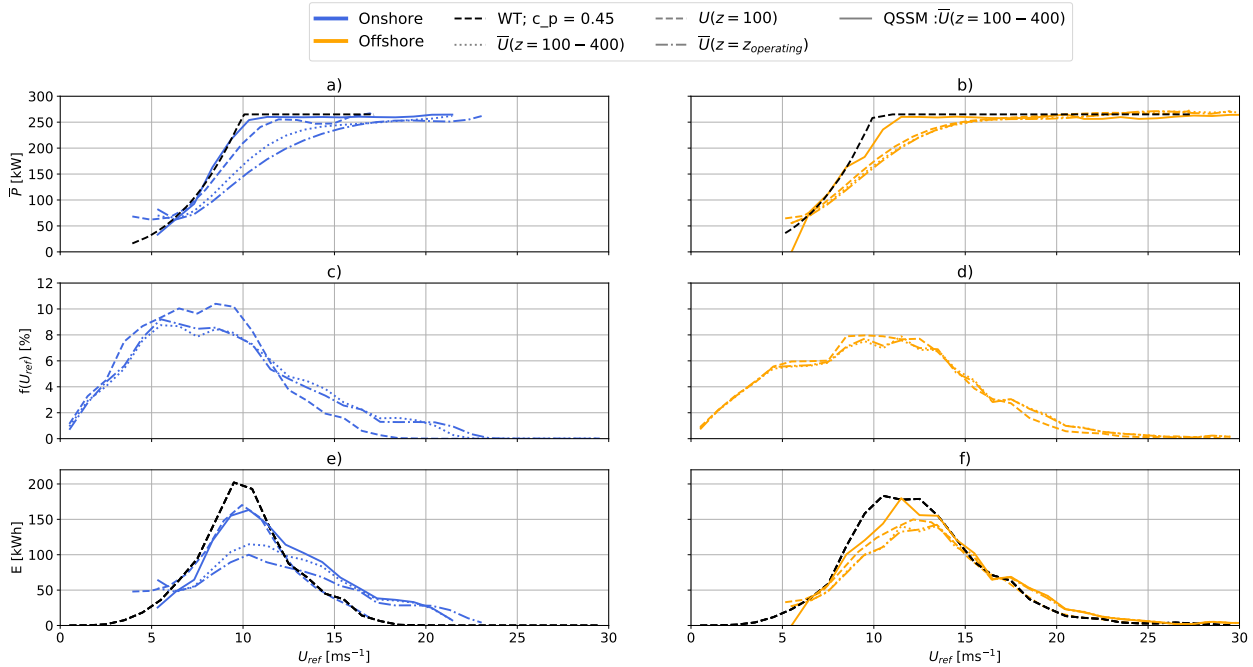


Figure 14. Onshore (blue) and offshore (orange) AWES power curves (a,b) over various reference wind speeds (dashed lines: fixed height $z = 100$ m; dotted lines: $z = 100 - 300$ m; dash-dotted lines: average wind speed along operating trajectory) based on 3 wind profiles for each of the $k=20$ clusters. A simplified WT (dashed black lines) and QSS AWES model (solid line) with same rated power are depicted as reference. Power curves and WRF-simulated annual wind speed probability distribution (c,d) for various reference heights result in annual energy production distribution (e,f) and AEP estimates.

The presented AWES and WT start producing significant power around $U \approx 5 \text{ ms}^{-1}$ and reach rated power between 12 and 15 ms^{-1} at their respective reference heights. Whereas the onshore AWES power curve with a fixed reference height of 100 m almost aligns with the power curve of a conventional wind turbine, other power curves are seemingly below that. This is likely
475 caused by higher wind shear and non-monotonic wind speed profiles which lead to faster winds aloft and higher operating altitudes with lower wind speeds at 100 m. For monotonically increasing wind speeds this leads to data points moving to the right when plotted against $u_{100-400m}$ in comparison to when they are plotted against u_{100m} . Offshore winds however experience less shear (see sub-section : 2.2), which is why offshore AWES power curves for any reference height almost overlap with each other. AWES energy production distribution is shifted towards higher wind speeds, particularly onshore, due
480 to higher average wind speeds at operating height. Furthermore, the distribution of AWES energy production shows a wider spread as the system operates within a wider range of wind speeds.

5.4 Annual Energy Production

Figure 15 shows AEP based on optimized power predictions for p5, p50, p95 wind velocity profiles within each of the $k = 5, 10, 20, 50$ clusters for 3 reference heights (AWES($z = 100\text{m}$), AWES($100\text{m} \leq z \leq 300\text{m}$), AWES(z_{oper})). These data are compared to QSS and WT reference models as well as optimized AWES performance estimates for logarithmic wind speed profiles (AWES_{log}($z = 100$)) and a Rayleigh distribution at 100 m. Additionally, AEP is assessed from a power summation (equation 10) over every n 10-min wind speed profile within each cluster k (AWES_{cluster}). For this approach, power $P_{i,j}^{\text{interp}}$ is interpolated between p5, p50 and p95 within each cluster and then added up to an annual total energy.

$$AEP = \sum_{j=1}^k \sum_{i=1}^n (P_{i,j}^{\text{interp}}) \quad (10)$$

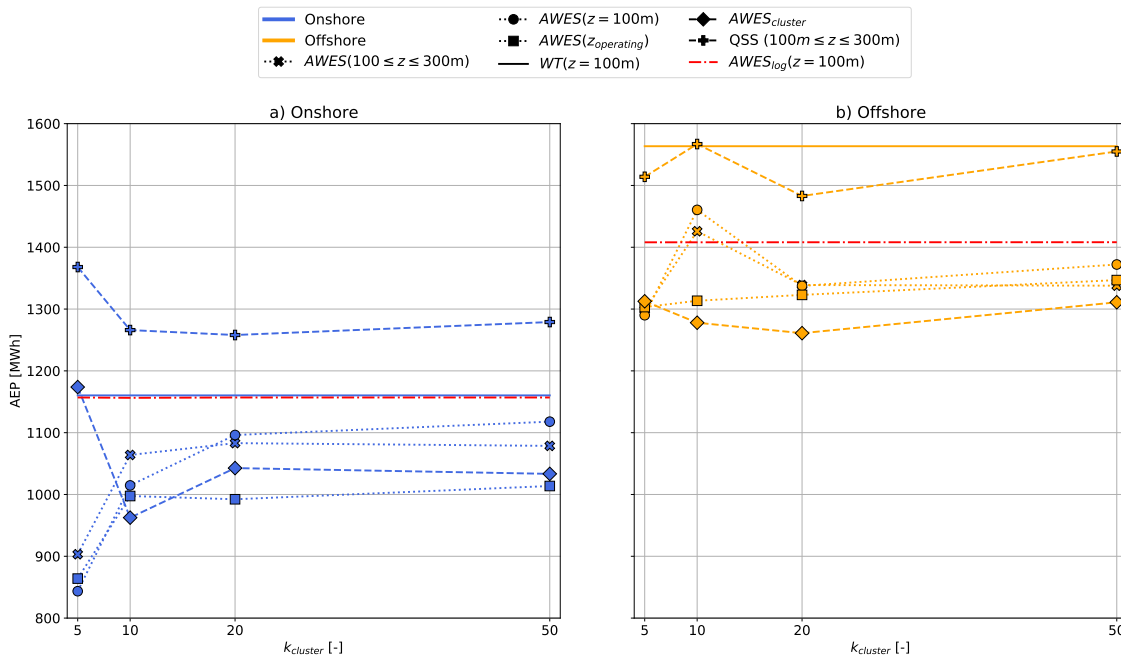


Figure 15. Onshore (a) and offshore (b) AEP over number of clusters k based on power curve and wind speed distribution in sub-section 5.3 over various reference heights. QSS (+) and WT (solid lines) reference models as well as optimized AWES performance estimated based on logarithmic wind speed profiles (red dash dotted lines) and a Rayleigh distribution at 100 m. AWES_{cluster} estimates AWES AEP based on the summation of interpolated power within each cluster.

Both onshore (blue) and offshore (orange) AEP vary with number of clusters, however above $k=20$ the variation is negligible and the possible improvement in energy prediction does not justify the increased computational cost. Less wind shear offshore results in decreased spread between reference heights. AEP predictions of AWES_{cluster} are generally lower than other estimates

and closest to $AWES(z_{operating})$, which could indicate that these are more realistic estimates. At both locations, the QSS model over predicts AEP, due to simplified assumptions. Onshore, QSS AEP is particularly high, because tether drag might not be accurately represented, favoring higher operating altitudes. The simplified WT model predicts higher powers than the dynamic optimization AWES model, particularly offshore where lower wind shear only slightly increases energy yield at higher altitudes. Logarithmic wind speed profiles 4.7 and Rayleigh wind speed probability distributions ($U_{onshore}^{ave} = 10 \text{ ms}^{-1}$ and $U_{offshore}^{ave} = 12 \text{ ms}^{-1}$) also predict higher AEP than WRF-simulated wind conditions. Offshore AEP estimates based on logarithmic wind profiles are closer to power curve estimates based on WRF data than similar onshore results. This implies that offshore wind conditions (wind profile shape and probability) are better represented by logarithmic wind speed profiles than onshore conditions.

6 Conclusions and outlook

We evaluated ground-generation AWES power, annual energy production, operating heights and tether lengths based on representative, mesoscale simulation data, as long-term high resolution high altitude measurements with sufficient data availability are scarce. This analysis uses onshore wind data at Pritzwalk in northern Germany and offshore wind data at the FINO3 research platform in the North Sea to drive AWES optimization toolbox (`awebox`) and generate power-optimized AWES trajectories. These simulations span an entire year with a temporal resolution of 10 minutes, thereby including seasonal, synoptic and diurnal variations at a higher resolution than re-analysis data sets. The annual wind roses for heights of 100 m and 500 m confirm the expected wind speed increase and clockwise rotation at both locations, with generally lower offshore wind shear and veer than onshore. Annual wind speed statistics reveal that while average wind speeds increase with height, low wind speeds still occur at a fairly high probability up to 1000 m.

To further dissect wind conditions essential to the design and operation of AWES and to reduce computational cost, a representative wind resource model is deduced using k-means clustered wind data. This algorithm groups similar profiles together into a fixed, predetermined number of k clusters represented by the mean of each cluster. For a representative k of 10 (chosen for visualization purposes) a more extensive analysis and comparison between onshore and offshore wind conditions revealed that average wind speed, rather than profile shape, plays a decisive role in assigning profiles to a certain cluster. However, the algorithm was able to identify and define a cluster for onshore LLJs as well as various non-logarithmic wind profiles at both locations. Individual clusters produce coherent groups of similar wind velocity profiles whose probability correlates with seasonal, diurnal and atmospheric stability variation. k-means clustering provides good insight into the wind regime, especially for higher altitudes where classification by Obukhov length is inadequate. Furthermore, the so derived clusters represent annual variation better than conventional logarithmic or exponential wind speed profiles.

Three representative wind velocity profiles based on the 5th, 50th and 95th percentiles within each cluster as well as logarithmic reference wind speed profiles were used as input into the airborne wind energy trajectory optimization toolbox `awebox` to estimate average cycle power of ground-generation AWES. A scaled Ampyx AP2 aircraft ($A_{wing} = 20 \text{ m}^2$) is analyzed in terms of trajectory, operating altitude, instantaneous tether force and length as well as power and AEP. AWESs at both

locations rarely operate above 300 m, with offshore systems mostly flying below 200 m, due to higher wind speeds at lower altitude and low wind shear. These results weaken the claim of increased power harvest above 500 m for AWES, but also obviate airspace restriction challenges for AWES. Simplified quasi-steady state (QSS) AWES as well as WT models were used to contextualize the optimization results and functioned as reference for power curve descriptions over various reference heights.

530 The WT model reach rated power at lower wind speeds, because tether losses decrease AWES power, which the QSS AWES model can not fully capture. Deriving AWES power curves from logarithmic wind speed profiles seems like a valid approach especially offshore. Logarithmic wind speed profiles onshore can not account for the high amount of non-monotonic profiles. Onshore, the choice of reference height can seemingly result in delayed rated power as the power curve shifts. This choice is less significant offshore due reduced wind shear and more monotonic wind velocity profiles. This choice highly affects AEP

535 predictions and requires further investigation.

Beneficial offshore wind conditions lead to higher AWES AEP than onshore. However, relative to the WT reference model, which generally predicts higher AEP, onshore AWES perform slightly better due to higher wind shear and higher wind speeds aloft. AEP estimates of the QSS AWES model are higher than dynamic optimization results, because they do not capture power variation along the flight path and under-predict tether losses. Probably the most realistic, but also lowest energy yield

540 predictions are derived from wind speed distributions at operating height $AWES_{operating}$ and the sum of interpolated power within each cluster $AWES_{cluster}$. AWES AEP based on logarithmic wind profiles and Rayleigh wind speed distributions predict higher yield than AEP based on clustered WRF-simulated wind resource, indicating that the conventional approach can not reproduce the impact of realistic wind conditions on AWES performance. This is due to the fact that the Rayleigh distribution over-predicts high wind speeds. Comparing WRF-clustered AEP for different power and wind resource descriptions

545 show that the benefits of using more than $k=20$ clusters are marginal while computational expense increases. Using the wind speed distribution at a fixed reference height of 100 m leads to an over prediction of annual energy, particularly onshore. A better reference could be average wind speed between 100 - 300 m because AWES mostly operate within this range and AEP estimates are closer to AEP of $AWES_{operating}$ and $AWES_{cluster}$. However, the choice of reference height for the derivation of the wind speed probability distribution is more important onshore, due to higher wind shear and more non-monotonic wind

550 speed profiles.

In summary, k-means clustering provides adequate categorization and realistic, representative wind velocity profiles for AWES trajectory optimization. This approach increases the accuracy of AWES power prediction in comparison to logarithmic wind speed profiles. Furthermore, clustering reduces the computational cost of power curve and AEP estimates as a low number of clusters suffices. Good AEP results and power curve description can be achieved by using multiple representative profiles

555 within each cluster.

Based on these results, we will describe the design space and weight budget of ground-generation AWES in a future sizing study using the clustered wind data. To that end, we will compare the performance of a high lift airfoil to the baseline AP2 aerodynamic reference model and determine the maximum permissible mass for different wing sizes. In the end, an investigation of measured power curves and real AEP from field trials is necessary to confirm or highlight deficiencies in the models used in

560 this paper. Until then, long-term AWES performance analysis based on mesoscale and reanalysis data could help determining

proper AWES AEP estimates. The description of the AWES wind resource, particularly onshore, needs further analysis as it highly impacts AWES energy yield predictions. An interesting open research question is the seasonality of AWES performance in comparison to WT.

6.1 Acknowledgments and funding sources

565 The authors thank the BMWi for funding of the “OnKites I” and “OnKites II” project [grant number 0325394A] on the basis of a decision by the German Bundestag and project management Projektträger Jülich. We thank the PICS, NSERC and the DAAD for their funding.

`awebox` has been developed in collaboration with the company Kiteswarms Ltd. The company has also supported the `awebox` project through research funding. The `awebox` project has received funding from the European Union’s Horizon
570 2020 research and innovation program under the Marie Skłodowska-Curie grant agreement No 642682 (AWESCO)

We thank the Carl von Ossietzky University of Oldenburg and the Energy Meteorology research group for providing access to their high performance computing cluster *EDDY* and ongoing support.

We further acknowledge Rachel Leuthold (University of Freiburg, SYSCOP) and Thilo Bronnenmeyer (Kiteswarms Ltd.) for their helped in writing this article, great, technical support and continued work on the `awebox`.

575 6.2 Author contribution

Markus Sommerfeld evaluated the data and wrote the manuscript in consultation and under the supervision of Curran Crawford. Martin Dörenkämper set up the numerical offshore simulation, contributed to the meteorological evaluation of the data and reviewed the manuscript. Jochem De Schutter co-developed the optimization model and helped writing and reviewed this manuscript.

580 References

- Ampyx: Ampyx Power BV, <https://www.ampyxpower.com/>, last accessed: 30.10.2020, 2020.
- Andersson, J. A. E., Gillis, J., Horn, G., Rawlings, J. B., and Diehl, M.: CasADi – A software framework for nonlinear optimization and optimal control, *Mathematical Programming Computation*, 11, 1–36, <https://doi.org/10.1007/s12532-018-0139-4>, 2019.
- Archer, C. L., Colle, B. A., Veron, D. L., Veron, F., and Sienkiewicz, M. J.: On the predominance of unstable atmospheric conditions in the marine boundary layer offshore of the U.S. northeastern coast, *Journal of Geophysical Research: Atmospheres*, 121, 8869–8885, <https://doi.org/10.1002/2016JD024896>, <https://agupubs.onlinelibrary.wiley.com/doi/abs/10.1002/2016JD024896>, 2016.
- Argatov, I. and Silvennoinen, R.: Efficiency of Traction Power Conversion Based on Crosswind Motion, pp. 65–79, Springer Berlin Heidelberg, Berlin, Heidelberg, https://doi.org/10.1007/978-3-642-39965-7_4, https://doi.org/10.1007/978-3-642-39965-7_4, 2013.
- Arya, P. and Holton, J.: Introduction to Micrometeorology, International Geophysics, Elsevier Science, 2001.
- 590 Aull, M., Stough, A., and Cohen, K.: Design Optimization and Sizing for Fly-Gen Airborne Wind Energy Systems, *Automation*, 1, 1–16, 2020.
- Banta, R. M.: Stable-boundary-layer regimes from the perspective of the low-level jet, *Acta Geophysica*, 56, 58–87, <https://doi.org/10.2478/s11600-007-0049-8>, <https://doi.org/10.2478/s11600-007-0049-8>, 2008.
- Bronnenmeyer, T.: Optimal Control for Multi-Kite Emergency Trajectories, Master’s thesis, University of Stuttgart, <https://cdn.syscop.de/publications/Bronnenmeyer2018.pdf>, 2018.
- 595 Cherubini, A., Papini, A., Verthey, R., and Fontana, M.: Airborne Wind Energy Systems: A review of the technologies, *Renewable and Sustainable Energy Reviews*, 51, 1461–1476, <https://doi.org/10.1016/j.rser.2015.07.053>, <http://linkinghub.elsevier.com/retrieve/pii/S1364032115007005>, 2015.
- De Schutter, J., Leuthold, R., and Diehl, M.: Optimal Control of a Rigid-Wing Rotary Kite System for Airborne Wind Energy, in: Proceedings of the European Control Conference (ECC), 2018.
- 600 De Schutter, J., Leuthold, R., Bronnenmeyer, T., Paelinck, R., and Diehl, M.: Optimal control of stacked multi-kite systems for utility-scale airborne wind energy, in: 2019 IEEE 58th Conference on Decision and Control (CDC), pp. 4865–4870, 2019.
- Dee, D. P., Uppala, S. M., Simmons, A. J., Berrisford, P., Poli, P., Kobayashi, S., Andrae, U., Balmaseda, M. A., Balsamo, G., Bauer, P., Bechtold, P., Beljaars, A. C. M., van de Berg, L., Bidlot, J., Bormann, N., Delsol, C., Dragani, R., Fuentes, M., Geer, A. J., Haimberger, L., Healy, S. B., Hersbach, H., Hólm, E. V., Isaksen, L., Kållberg, P., Köhler, M., Matricardi, M., McNally, A. P., Monge-Sanz, B. M., Morcrette, J.-J., Park, B.-K., Peubey, C., de Rosnay, P., Tavolato, C., Thépaut, J.-N., and Vitart, F.: The ERA-Interim reanalysis: configuration and performance of the data assimilation system, *Quarterly Journal of the Royal Meteorological Society*, 137, 553–597, <https://doi.org/10.1002/qj.828>, 2011.
- Diehl, M.: Airborne Wind Energy: Basic Concepts and Physical Foundations, in: *Airborne Wind Energy*, edited by Ahrens, U., Diehl, M., and Schmehl, R., pp. 3–22, Springer Berlin Heidelberg, Berlin, Heidelberg, https://doi.org/10.1007/978-3-642-39965-7_1, https://doi.org/10.1007/978-3-642-39965-7_1, 2013.
- 610 Donlon, C. J., Martin, M., Stark, J., Roberts-Jones, J., Fiedler, E., and Wimmer, W.: The Operational Sea Surface Temperature and Sea Ice Analysis (OSTIA) system, *Remote Sensing of Environment*, 116, 140–158, <https://doi.org/10.1016/j.rse.2010.10.017>, 2012.
- Dörenkämper, M., Optis, M., Monahan, A., and Steinfeld, G.: On the Offshore advection of Boundary-Layer Structures and the Influence on Offshore Wind Conditions, *Boundary-Layer Meteorol.*, 155, 459–482, <https://doi.org/10.1007/s10546-015-0008-x>, 2015.

- Dörenkämper, M., Stoevesandt, B., and Heinemann, D.: Derivation of an offshore wind index for the German bight from high-resolution mesoscale simulation data, *Proceedings of DEWEK - German Offshore Wind Energy Conference*, p. 5, 2017.
- Dörenkämper, M., Olsen, B. T., Witha, B., Hahmann, A. N., Davis, N. N., Barcons, J., Ezber, Y., García-Bustamante, E., González-Rouco, J. F., Navarro, J., Sastre-Marugán, M., Sile, T., Trei, W., Žagar, M., Badger, J., Gottschall, J., Sanz Rodrigo, J., and Mann, J.: The Making of the New European Wind Atlas – Part 2: Production and evaluation, *Geoscientific Model Development*, 13, 5079–5102, <https://doi.org/10.5194/gmd-13-5079-2020>, <https://gmd.copernicus.org/articles/13/5079/2020/>, 2020.
- Echeverri, P., Fricke, T., Homsy, G., and Tucker, N.: The Energy Kite - Selected Results From the Design, Development and Testing of Makani's Airborne Wind Turbines - Part 1, Technical Report 1, Makani Power, https://storage.googleapis.com/x-prod.appspot.com/files/Makani_TheEnergyKiteReport_Part1.pdf, 2020.
- Eijkelhof, D., Rapp, S., Fasel, U., Gaunaa, M., and Schmehl, R.: Reference Design and Simulation Framework of a Multi-Megawatt Airborne Wind Energy System, *Journal of Physics: Conference Series*, 1618, 032 020, <https://doi.org/10.1088/1742-6596/1618/3/032020>, <https://doi.org/10.1088/1742-6596/1618/3/032020>, 2020.
- Emeis, S.: *Wind energy meteorology: atmospheric physics for wind power generation*, Springer, Heidelberg, 2018.
- Fagiano, L. and Milanese, M.: Airborne Wind Energy: An overview, in: 2012 American Control Conference (ACC), pp. 3132–3143, <https://doi.org/10.1109/ACC.2012.6314801>, 2012.
- Floors, R., Batchvarova, E., Gryning, S.-E., Hahmann, A. N., Peña, A., and Mikkelsen, T.: Atmospheric boundary layer wind profile at a flat coastal site - wind speed lidar measurements and mesoscale modeling results, *Advances in Science and Research*, 6, 155–159, <https://doi.org/10.5194/asr-6-155-2011>, <http://www.adv-sci-res.net/6/155/2011/>, 2011.
- Gros, S., Zanon, M., and Diehl, M.: A relaxation strategy for the optimization of airborne wind energy systems, in: Control Conference (ECC), 2013 European, pp. 1011–1016, IEEE, http://ieeexplore.ieee.org/xpls/abs_all.jsp?arnumber=6669670, 2013.
- Haas, T., Schutter, J. D., Diehl, M., and Meyers, J.: Wake characteristics of pumping mode airborne wind energy systems, *Journal of Physics: Conference Series*, 1256, 012 016, <https://doi.org/10.1088/1742-6596/1256/1/012016>, <https://doi.org/10.1088/1742-6596/1256/1/012016>, 2019.
- Hahmann, A. N., Sile, T., Witha, B., Davis, N. N., Dörenkämper, M., Ezber, Y., García-Bustamante, E., González-Rouco, J. F., Navarro, J., Olsen, B. T., and Söderberg, S.: The making of the New European Wind Atlas – Part 1: Model sensitivity, *Geoscientific Model Development*, 13, 5053–5078, <https://doi.org/10.5194/gmd-13-5053-2020>, <https://gmd.copernicus.org/articles/13/5053/2020/>, 2020.
- Hersbach, H. and Dick, D.: ERA5 reanalysis is in production, <http://www.ecmwf.int/en/newsletter/147/news/era5-reanalysis-production>, last accessed: 22.10.2019, 2016.
- Houska, B. and Diehl, M.: Optimal control for power generating kites, in: 2007 European Control Conference (ECC), pp. 3560–3567, <https://doi.org/10.23919/ECC.2007.7068861>, 2007.
- HSL: The HSL Mathematical Software Library @ONLINE, <http://www.hsl.rl.ac.uk/>, 2020.
- International Electrotechnical Commission, ed.: Design requirements: amendment 1, no. 1,1 in *Wind turbines*, IEC, Geneva, ed. 3.0, 2010-10 edn., oCLC: 838280539, 2010.
- Kruijff, M. and Ruiterkamp, R.: A Roadmap Towards Airborne Wind Energy in the Utility Sector, pp. 643–662, Springer Singapore, Singapore, https://doi.org/10.1007/978-981-10-1947-0_26, https://doi.org/10.1007/978-981-10-1947-0_26, 2018.
- Leuthold, R., De Schutter, J., Malz, E. C., Licitra, G., Gros, S., and Diehl, M.: Operational Regions of a Multi-Kite AWE System, in: 2018 European Control Conference (ECC), pp. 52–57, <https://doi.org/10.23919/ECC.2018.8550199>, 2018.

- Leuthold, R., De Schutter, J., Malz, E., Licitra, G., Bronnenmeyer, T., Gros, S., and Diehl, M.: *awebox*: Modelling and optimal control of single- and multiple-kite systems for airborne wind energy, <https://github.com/awebox>, 2020.
- 655 Licitra, G., Koenemann, J., Bürger, A., Williams, P., Ruiterkamp, R., and Diehl, M.: Performance assessment of a rigid wing Airborne Wind Energy pumping system, *Energy*, 173, 569–585, <https://doi.org/10.1016/j.energy.2019.02.064>, 2019.
- Loyd, M. L.: Crosswind kite power (for large-scale wind power production), *Journal of energy*, 4, 106–111, <http://arc.aiaa.org/doi/abs/10.2514/3.48021>, 1980.
- Lunney, E., Ban, M., Duic, N., and Foley, A.: A state-of-the-art review and feasibility analysis of high altitude wind power in Northern Ireland, *Renewable and Sustainable Energy Reviews*, 68, 899 – 911, <https://doi.org/https://doi.org/10.1016/j.rser.2016.08.014>, <http://www.sciencedirect.com/science/article/pii/S1364032116304282>, 2017.
- 660 Malz, E., Koenemann, J., Sieberling, S., and Gros, S.: A reference model for airborne wind energy systems for optimization and control, *Renewable Energy*, 140, 1004 – 1011, <https://doi.org/https://doi.org/10.1016/j.renene.2019.03.111>, <http://www.sciencedirect.com/science/article/pii/S0960148119304239>, 2019.
- 665 Malz, E., Hedenus, F., Göransson, L., Verendel, V., and Gros, S.: Drag-mode airborne wind energy vs. wind turbines: An analysis of power production, variability and geography, *Energy*, 193, 116 765, <https://doi.org/https://doi.org/10.1016/j.energy.2019.116765>, <http://www.sciencedirect.com/science/article/pii/S0360544219324600>, 2020.
- Molina-García, A., Fernández-Guillamón, A., Gómez-Lázaro, E., Honrubia-Escribano, A., and Bueso, M. C.: Vertical Wind Profile Characterization and Identification of Patterns Based on a Shape Clustering Algorithm, *IEEE Access*, 7, 30 890–30 904, <https://doi.org/10.1109/ACCESS.2019.2902242>, 2019.
- 670 Nakanishi, M. and Niino, H.: Development of an Improved Turbulence Closure Model for the Atmospheric Boundary Layer, *Journal of the Meteorological Society of Japan*, 87, 895–912, <https://doi.org/10.2151/jmsj.87.895>, 2009.
- Obukhov, A. M.: Turbulence in an atmosphere with a non-uniform temperature, *Boundary-Layer Meteorology*, 2, 7–29, <https://doi.org/10.1007/BF00718085>, 1971.
- 675 Olauson, J.: ERA5: The new champion of wind power modelling?, *Renewable Energy*, 126, 322–331, <https://doi.org/10.1016/j.renene.2018.03.056>, 2018.
- Optis, M., Monahan, A., and Bosveld, F. C.: Limitations and breakdown of Monin–Obukhov similarity theory for wind profile extrapolation under stable stratification, *Wind Energy*, 19, 1053–1072, <https://doi.org/10.1002/we.1883>, 2016.
- Peña, A., Gryning, S.-E., and Floors, R.: Lidar observations of marine boundary-layer winds and heights: a preliminary study, *Meteorologische Zeitschrift*, 24, 581–589, <https://doi.org/10.1127/metz/2015/0636>, http://www.schweizerbart.de/papers/metz/detail/24/84892/Lidar_observations_of_marine_boundary_layer_winds_?af=crossref, 2015.
- 680 Pedregosa, F., Varoquaux, G., Gramfort, A., Michel, V., Thirion, B., Grisel, O., Blondel, M., Prettenhofer, P., Weiss, R., Dubourg, V., Vanderplas, J., Passos, A., Cournapeau, D., Brucher, M., Perrot, M., and Duchesnay, E.: Scikit-learn: Machine Learning in Python, *Journal of Machine Learning Research*, 12, 2825–2830, 2011.
- 685 Salvação, N. and Guedes Soares, C.: Wind resource assessment offshore the Atlantic Iberian coast with the WRF model, *Energy*, 145, 276 – 287, <https://doi.org/https://doi.org/10.1016/j.energy.2017.12.101>, <http://www.sciencedirect.com/science/article/pii/S0360544217321448>, 2018.
- Schelbergen, M., Kalverla, P. C., Schmehl, R., and Watson, S. J.: Clustering wind profile shapes to estimate airborne wind energy production, *Wind Energy Science*, 5, 1097–1120, <https://doi.org/10.5194/wes-5-1097-2020>, <https://wes.copernicus.org/articles/5/1097/2020/>, 2020a.

- 690 Schelbergen, M., Kalverla, P. C., Schmehl, R., and Watson, S. J.: Clustering wind profile shapes to estimate airborne wind energy production, *Wind Energy Science Discussions*, 2020, 1–34, <https://doi.org/10.5194/wes-2019-108>, <https://www.wind-energ-sci-discuss.net/wes-2019-108/>, 2020b.
- Schmehl, R., Noom, M., and van der Vlugt, R.: Traction Power Generation with Tethered Wings, pp. 23–45, Springer Berlin Heidelberg, Berlin, Heidelberg, https://doi.org/10.1007/978-3-642-39965-7_2, https://doi.org/10.1007/978-3-642-39965-7_2, 2013.
- 695 Sempreviva, A. M. and Gryning, S.-E.: Humidity fluctuations in the marine boundary layer measured at a coastal site with an infrared humidity sensor, *Boundary-Layer Meteorology*, 77, 331–352, <https://doi.org/10.1007/BF00123531>, 1996.
- Skamarock, W., Klemp, J., Dudhia, J., Gill, D., Barker, D., Duda, M., Huang, X., Wang, W., and Powers, J.: A description of the advanced research WRF version 3, Tech. Rep. NCAR/TN–475+STR, NCAR - National Center for Atmospheric Research, Boulder, Colorado, USA, <http://n2t.net/ark:/85065/d72n51q1>, 2008.
- 700 Sommerfeld, M., Crawford, C., Monahan, A., and Bastigkeit, I.: LiDAR-based characterization of mid-altitude wind conditions for airborne wind energy systems, *Wind Energy*, 22, 1101–1120, <https://doi.org/10.1002/we.2343>, 2019a.
- Sommerfeld, M., Dörenkämper, M., Steinfeld, G., and Crawford, C.: Improving mesoscale wind speed forecasts using lidar-based observation nudging for airborne wind energy systems, *Wind Energy Science*, 4, 563–580, <https://doi.org/10.5194/wes-4-563-2019>, <https://www.wind-energ-sci.net/4/563/2019/>, 2019b.
- 705 Stull, R.: *An Introduction to Boundary Layer Meteorology*, Atmospheric and Oceanographic Sciences Library, Springer Netherlands, <https://books.google.ca/books?id=eRRz9RNvNOKC>, 1988.
- van der Vlugt, R., Bley, A., Noom, M., and Schmehl, R.: Quasi-steady model of a pumping kite power system, *Renewable Energy*, 131, 83–99, <https://doi.org/10.1016/j.renene.2018.07.023>, <http://www.sciencedirect.com/science/article/pii/S0960148118308206>, 2019.
- Wächter, A. and Biegler, L. T.: On the implementation of an interior-point filter line-search algorithm for large-scale nonlinear programming, *Mathematical Programming*, 106, 25–57, <https://doi.org/10.1007/s10107-004-0559-y>, <https://doi.org/10.1007/s10107-004-0559-y>, 2006.
- 710

Appendix A: Figures

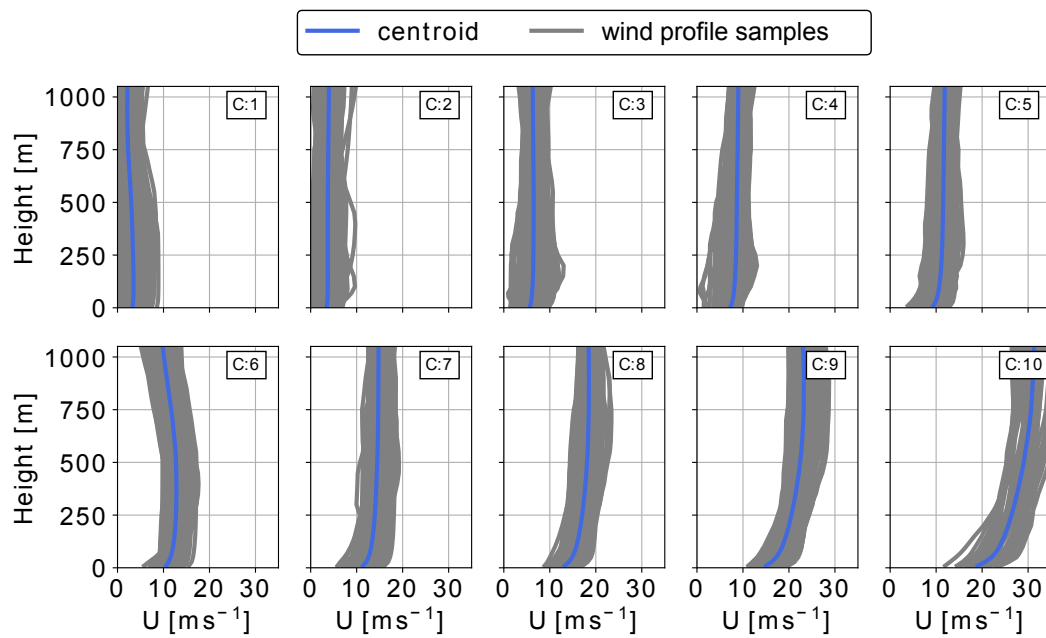


Figure A1. clustered offshore wind velocity profiles (here shown as 2D projected wind speed profiles). The average profile or centroid is shown in blue while all the assigned profiles are shown in grey.

onshore; k=10 clusters

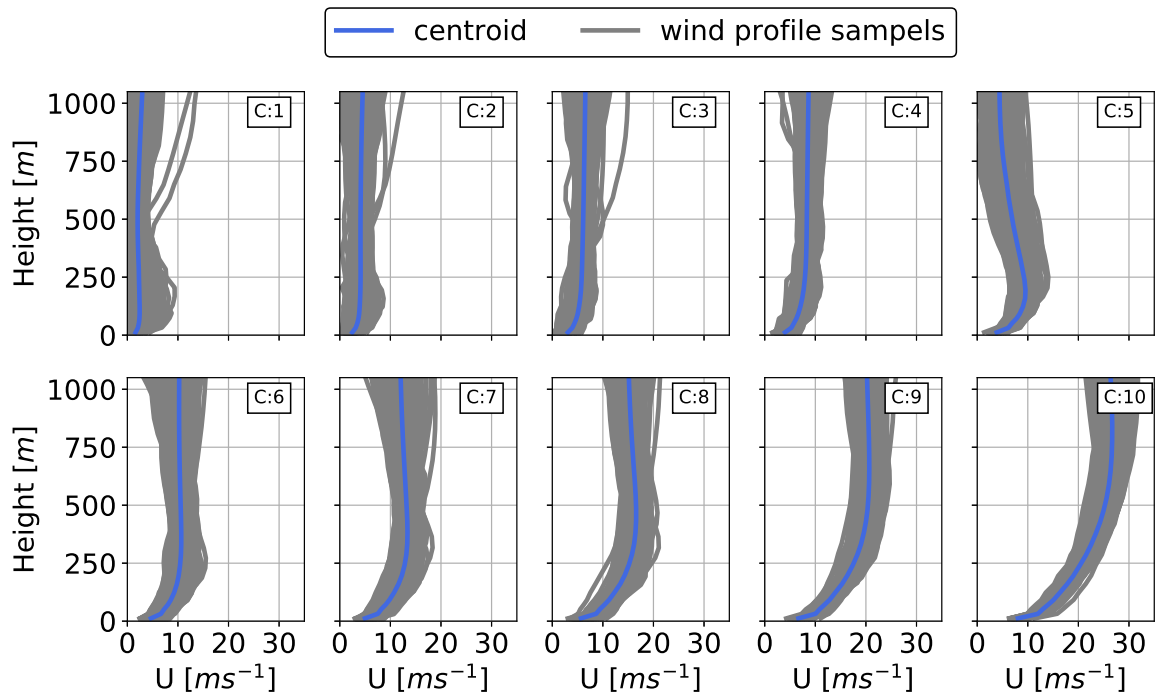


Figure A2. Clustered offshore wind velocity profiles (here shown as wind speed profiles). The average profile or centroid is shown in blue while all the assigned profiles are shown in grey.

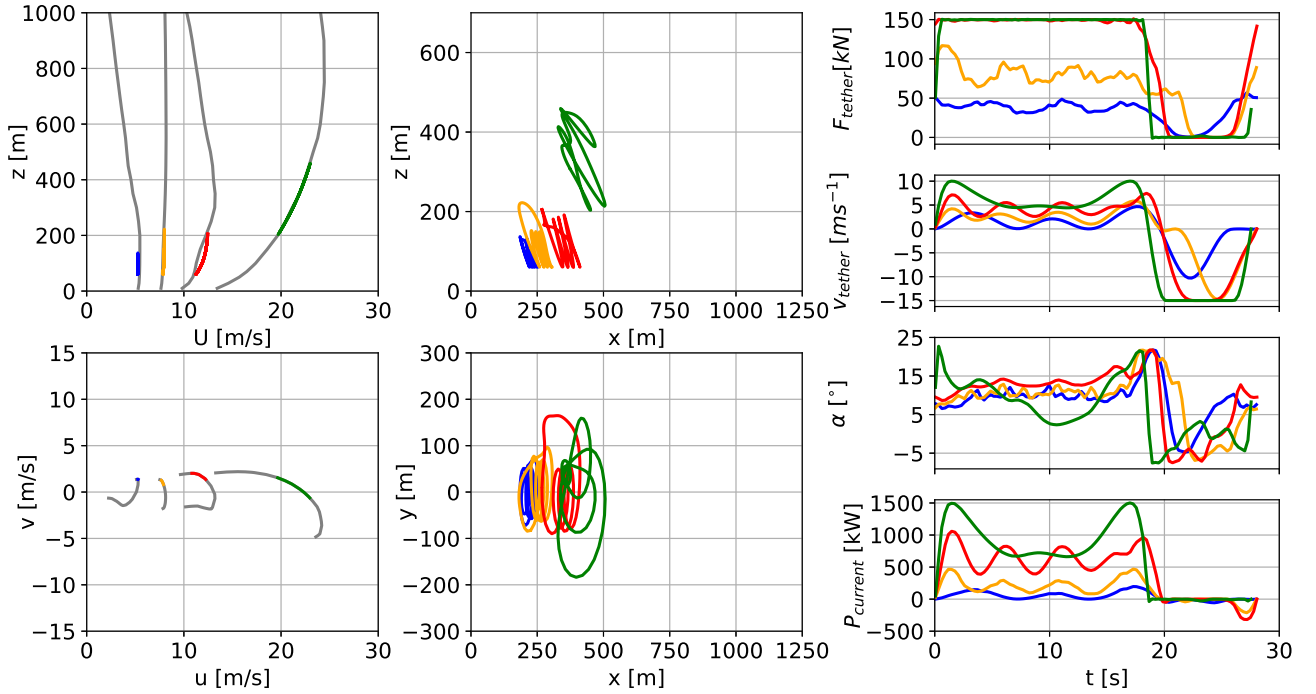


Figure A3. Representative wind speed profiles (left, top), and hodograph (top view) of wind velocity up to 1000 m (left, bottom). The deviation of the colored lines is caused by the approximation of discrete data points with Lagrange polynomials. Trajectories (center) in side and top view. Temporal variations of tether force F_{tether} (right, 1st from top), tether speed v_{tether} (right, 2nd from top), angle of attack α (right, 3rd from top) and instantaneous power P_{current} (right, bottom) optimized based on clustered offshore wind speed profiles for a ground-generation aircraft with a wing area of $A_{\text{wing}} = 20 \text{ m}^2$.

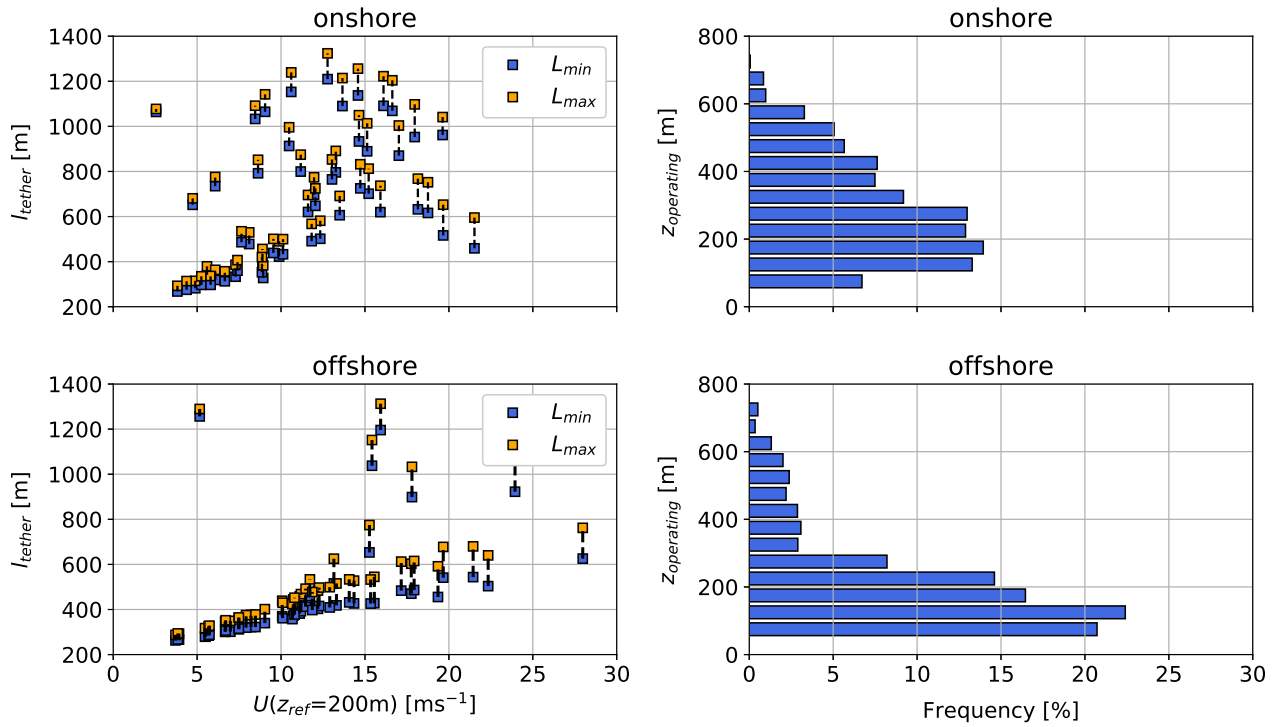


Figure A4. Tether length range (left) over reference wind speed $U(z_{ref} = 200 \text{ m})$ and frequency distribution of operating altitude (right) based on $k=20$ onshore (top) and offshore (bottom) clusters for a ground-generation aircraft with a wing area of $A_{wing} = 50 \text{ m}^2$.

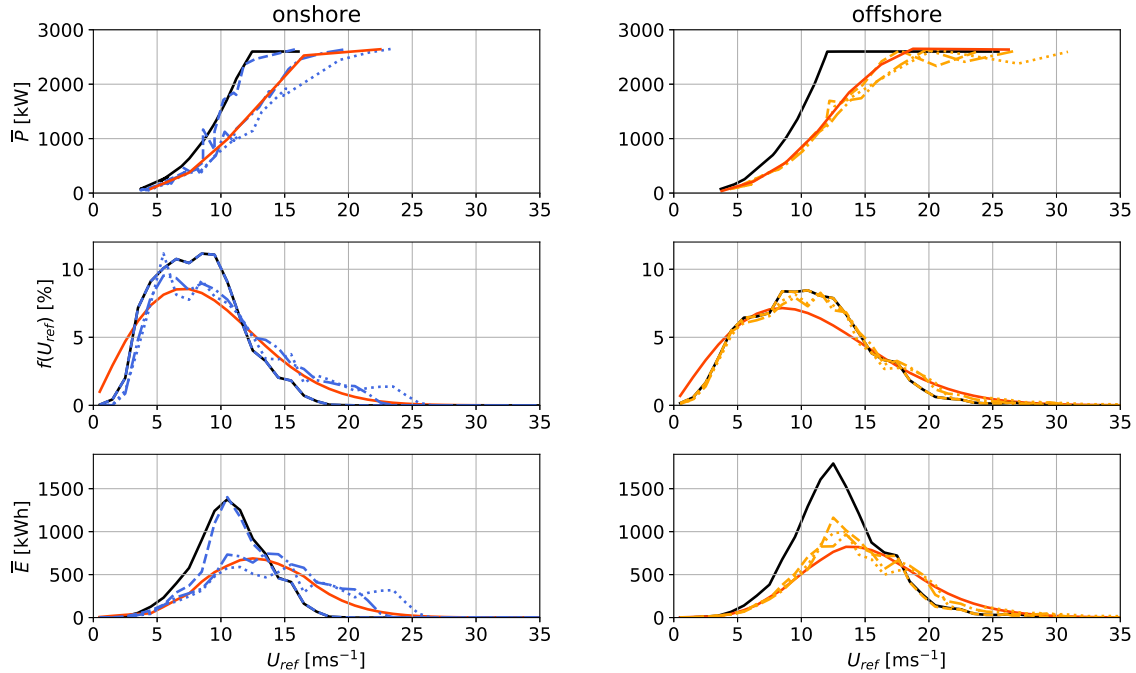
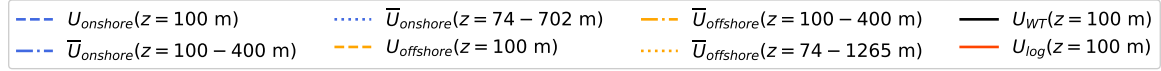


Figure A5. AWES power curves onshore (top left, blue) and offshore (top right, orange) for $A_{wing} = 50 \text{ m}^2$ over various reference wind speed height definitions (dashed lines: fixed height $z = 100\text{m}$; dash-dotted lines: fixed height range $z = 100 - 400 \text{ m}$; dotted lines: average wind speed along operating trajectory) based on 3 profiles for each of the $k=20$ clusters. Compared to WT (black) with same rated power at a hub height of $z_{WT} = 100 \text{ m}$ and AWES (red) for logarithmic wind speed profiles ($z_0 = 0.1$ onshore and $z_0 = 0.001$ offshore). Annual wind speed probability distribution (center) based on WRF simulation and Rayleigh distribution (red) with $U_{ave} = 10 \text{ ms}^{-1}$ (onshore) and 12 ms^{-1} (offshore) for reference. Energy production distribution (bottom) shows the distribution of annual produced energy over wind speed which is the product of power and wind speed probability distribution. Integrating this product results in the AEP.

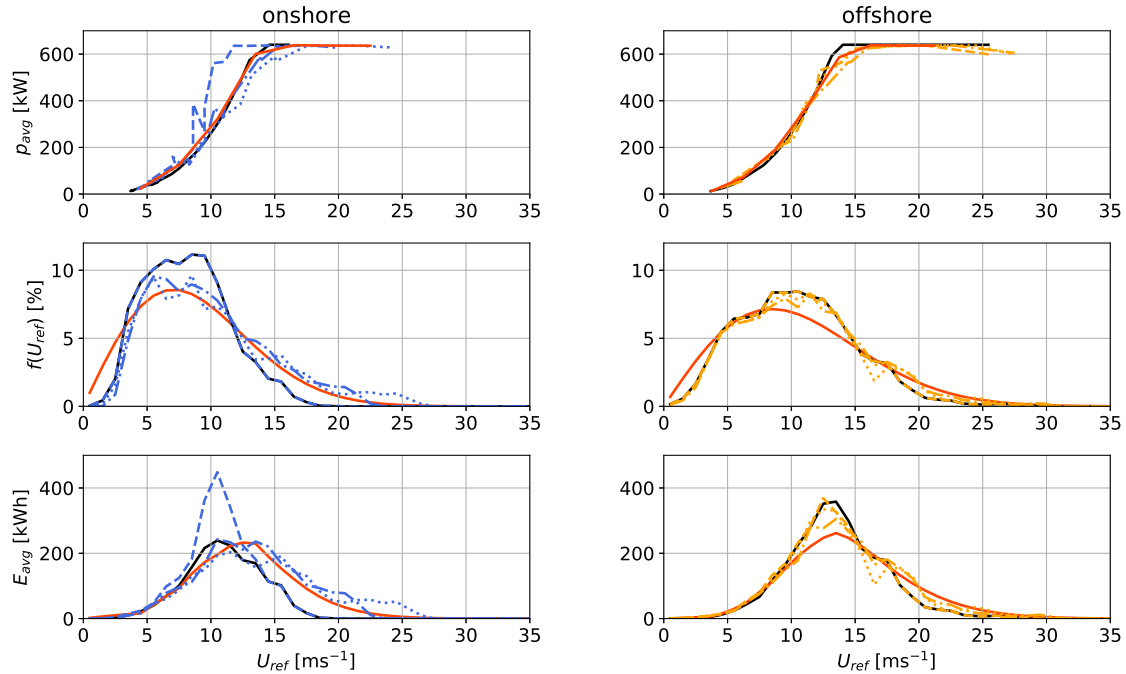
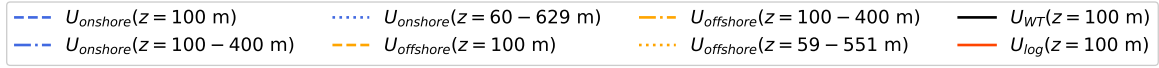


Figure A6. AWES power curves onshore (top left, blue) and offshore (top right, orange) for $A_{wing} = 50 \text{ m}^2$ over various reference wind speed height definitions (dashed lines: fixed height $z = 100$ m; dash-dotted lines: fixed height range $z = 100 - 400$ m; dotted lines: average wind speed along operating trajectory) based on 3 profiles for each of the $k=20$ clusters. Compared to WT (black) with $c_p^{WT} = 0.3$ and same rated power at a hub height of $z_{WT} = 100$ m and AWES (red) for logarithmic wind speed profiles ($z_0 = 0.1$ onshore and $z_0 = 0.001$ offshore). Annual wind speed probability distribution (center) based on WRF simulation and Rayleigh distribution (red) with $U_{ave} = 10 \text{ ms}^{-1}$ (onshore) and 12 ms^{-1} (offshore) for reference. Energy production distribution (bottom) shows the distribution of annual produced energy over wind speed which is the product of power and wind speed probability distribution. Integrating this product results in the AEP.